

1 **Impacts of waves and sea states on air-sea momentum**
2 **flux in the Northwest Tropical Atlantic Ocean:**
3 **parameterization and wave coupled climate modeling**

4 **César Sauvage¹, Hyodae Seo¹, Carol Anne Clayson¹, and James B. Edson¹.**

5 ¹Woods Hole Oceanographic Institution, Woods Hole, Massachusetts, USA

6 **Key Points:**

- 7 • Surface stress at moderate to high winds is dominated by short wind waves.
8 • COARE3.5 wave based formulation overestimates swell impact on the surface
9 stress in mixed sea conditions.
10 • Using the mean wave period or including the directional alignment between
11 wind and wave in COARE3.5 alleviates this issue.

Corresponding author: César Sauvage, csauvage@whoi.edu

Abstract

In winter, the Northwest Tropical Atlantic Ocean can be characterized by various regimes of interactions among ocean current, surface wind, and wind waves, which are critical for accurately describing surface wind stress. In this work, coupled wave-ocean-atmosphere model simulations are conducted using two different wave roughness parameterizations within COARE3.5, including one that relies solely on wind speed and another that uses wave age and wave slope as inputs. Comparisons with the directly measured momentum fluxes during the ATOMIC/EUREC⁴A experiments in winter 2020 show that, for sea states dominated by short wind waves under moderate to strong winds, the wave-based formulation increases the surface roughness length by 40% compared to the wind-speed-based approach. For sea states dominated by remotely generated swells under moderate to strong wind intensity, the wave-based formulation predicts significantly lower roughness length and surface stress ($\approx 20\%$), resulting in increased near-surface wind speed above the constant flux layer ($\approx 5\%$). Further investigation of the mixed sea states in the model and data indicates that the impact of swell on wind stress is over-emphasized in the COARE3.5 wave-based formulation, especially under moderate wind regimes. Various approaches are explored to alleviate this deficiency by either introducing directional alignment between wind and waves or using the mean wave period instead of the wave period corresponding to the spectral peak to compute the wave age.

Plain Language Summary

Accurately understanding and describing air-sea interactions is critical for weather forecast and regional climate. In this work, we use numerical experiments with and without taking into account the ocean waves to describe air-sea interactions. Most of the momentum exchange between the ocean and the atmosphere is done through locally wind-generated waves, however remotely generated waves, such as swells, can also interfere in these air-sea interaction. Comparisons with observations made during the ATOMIC/EUREC⁴A field campaigns in winter 2020 show in particular that our numerical experiment overestimated the impact of the swell on the atmosphere. Various approaches are explored here to alleviate this deficiency, one of those being the introduction of the effect of the alignment between wind and waves.

1 Introduction

Over the ocean, most of the momentum, heat, and mass exchanges with the atmosphere are supported by short wind-waves on spatial scales of $O(0.1-10\text{m})$. These wind-waves enhance the surface drag and roughness at the air-sea interface, thereby increasing the wind stress. The wind stress is coupled with the planetary boundary layer (PBL) processes in the atmosphere, modifying the kinematic and thermodynamic profiles in this lowest part of the atmosphere (Janssen, 1989; Moon et al., 2004). In addition to locally generated wind-waves, the sea state is also influenced by the remotely generated swell, especially in the lower latitudes, whose propagation direction is often uncorrelated with local winds. The fast-propagating swell wave that is strongly misaligned with or outruns the local wind can be a conduit for upward momentum and energy transfer from waves to the wind, forming a wave-driven low-level jet (e.g., Harris, 1966; Sullivan et al., 2008; Hanley & Belcher, 2008) and dissipating the swell waves (Donelan, 1999; Kahma et al., 2016; Liu et al., 2017).

In the atmospheric models, the wind stress over the oceans is parameterized in the surface-layer scheme using bulk formulas, such as the Coupled Ocean-Atmosphere Response Experiment (COARE, Fairall et al., 1996, 2003; Edson et al., 2013). If no coincident wave fields are available, COARE parameterizes the wave

roughness length (z_0) using wind speeds only. In this study, this approach will be referred to as the wind-speed-dependent formulation (WSDF). Since wind and wind-waves are in near-equilibrium in many cases over the extratropical open oceans, the COARE’s WSDF accurately parameterizes the surface roughness and thereby the surface stress (Edson et al., 2013). However, under low-wind regimes, especially in the tropics such as our study region, where longer waves and swell may not be in equilibrium with the local winds, wind speed alone is insufficient to describe the wave impact on the surface stress and surface roughness. To improve estimates of the fluxes under these conditions, “wave-based” formulations exist in many bulk flux algorithms that model z_0 as a function of wave age or wave age/slope (e.g., Taylor & Yelland, 2001; Oost et al., 2002; Drennan et al., 2003; Edson et al., 2013; Sauvage et al., 2020). As there are increasing interests and opportunities to incorporate the wave effects on surface fluxes in numerical models, such wave-based formulations (WBF) in bulk formulas will likely be adopted more in such models. It is, then, imperative to understand the challenges and deficiencies in current WBFs and offer possible revisions to the formulations for air-sea fluxes with increased accuracy. The goal of this paper is to enhance a regime-based understanding of wave-wind interactions via detailed validation of the parameterized air-sea flux from high-resolution coupled model simulations against directly measured air-sea fluxes.

This study focuses on air-sea momentum flux during the ATOMIC/EUREC⁴A field campaign. The ATOMIC (Atlantic Tradewind Ocean-Atmosphere Mesoscale Interaction Campaign) is the U.S. complement to the European field campaign, EUREC⁴A (Elucidating the Role of Cloud-Circulation Coupling in Climate, Stevens et al., 2021), both of which took place in the Northwest Tropical Atlantic Ocean in January-February 2020 (Figure 1). The primary objective of this study is to determine how well the current WBF in an advanced bulk flux algorithm such as COARE3.5 reproduces the observed wind stress in the mixed sea conditions compared to the WSDF. By exploiting the fully-coupled ocean-atmosphere-wave model simulations and extensive analyses of the in situ observational datasets, we will attempt to explain the causes for discrepancies between simulated and measured wind stresses. Our results indicate that the current COARE3.5 WBF underestimates z_0 and wind stress, particularly over the mixed sea state. We will show that this is due to either a missing physics of the wave-wind interaction or using an inappropriate wave input parameter to describe the mixed sea condition. This will rectify these problems by accounting for the missing physics or refining the wave input parameters in the formulations used in the current COARE3.5 WBF.

The paper is organized as follows. Section 2 describes the technical details of the latest z_0 formulation in COARE3.5. Sections 2b,c discuss the fully coupled ocean-atmosphere-wave modeling system used in the investigation, followed by the details on the experimental design and observational datasets in Section 2d and Section 2f, respectively. The wave impact on z_0 , wind stress, and low-level winds are discussed in a case study investigation in Section 3. Section 4 provides an in-depth comparison of the parameterized momentum flux against the direct measurements, identifying the areas and regimes for further improvement. In section 5, possible approaches are proposed and tested to alleviate the biases. Section 6 provides a summary and discussion.

2 Air-sea flux parameterization and coupled model

The interaction across the air-sea interface determines the turbulent exchanges of heat, moisture, and momentum, which are typically parameterized in atmospheric, ocean, and wave models using bulk aerodynamic formulas. This section provides a brief overview of the wave-mediated momentum flux implemented in

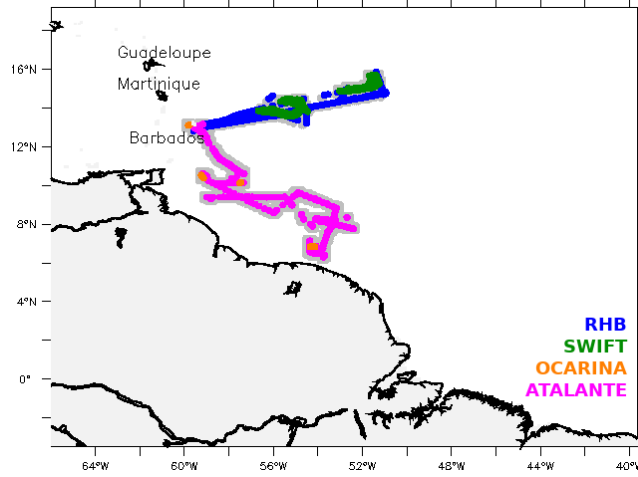


Figure 1. Tracks of the different platforms measuring surface stress (see more details in Section 2.5). The gray area denotes where the model outputs are sampled along the tracks of observations.

113 the Coupled Ocean-Atmosphere Response Experiment parameterization (COARE,
114 Fairall et al., 1996, 2003; Edson et al., 2013).

115 2.1 Roughness length and momentum flux in COARE3.5

116 The along wind stress in the COARE framework is defined as:

$$\tau = \rho C_D(z, z_0, \psi_m) U_r(z) S_r(z) = \rho u_*^2, \quad (1)$$

117 where ρ_a is the air density, $U_r(z)$ is the magnitude of the along-wind component
118 of the wind vector, $S_r(z)$ is the scalar wind speed, where the subscript r denotes
119 relative to the ocean surface; and u_* the friction velocity. C_D is the drag coefficient
120 defined as:

$$C_D(z, z_0, \psi_m) = \left[\frac{\kappa}{\ln(z/z_0) - \psi_m(\zeta)} \right]^2, \quad (2)$$

121 where κ is the von Kármán constant, $\psi_m(\zeta)$ is an empirical function of at-
122 mospheric stability, ζ is the z/L ratio with L the Obukhov length and z the height
123 above the surface (Fairall et al., 1996). The surface roughness length z_0 is param-
124 eterized in COARE3.5 as the sum of two terms:

$$z_0 = z_0^{smooth} + z_0^{rough}, \quad (3)$$

125 where z_0^{smooth} and z_0^{rough} represent the smooth and rough flow components of
126 z_0 , respectively (Edson et al., 2013). The smooth flow component is parameterized
127 as

$$z_0^{smooth} = \gamma \frac{\nu}{u_*}, \quad (4)$$

128 where γ is the roughness Reynolds number for smooth flow, set to be con-
 129 stant at 0.11 based on laboratory experiments, and ν is the kinematic viscos-
 130 ity. For smooth flow, the wind stress is mainly supported by viscous stress where
 131 $z_0 \approx z_0^{smooth}$.

132 The rough part of the roughness length, z_0^{rough} , is meant to parameterize the
 133 wind-driven gravity waves that support most of the stress above approximately 5
 134 ms^{-1} when the sea becomes aerodynamically rough. This component of the rough-
 135 ness is formulated currently in several ways in COARE3.5. The simplest and the
 136 most broadly used way is to parameterize it as a function of wind speed only. The
 137 so-called wind speed dependent formulation without explicit wave and sea states
 138 inputs estimates z_0^{rough} using the Charnock's relation (Charnock, 1955):

$$z_0^{rough} = \frac{\alpha_{ch} u_*^2}{g}, \quad (5)$$

139 where g is the acceleration of gravity and α_{CH} is the Charnock coefficient that
 140 is dependent only on wind speed. COARE3.5 formulates α_{CH} as

$$\alpha_{ch} = mU_{r10N} + b, \quad (6)$$

141 where U_{r10N} is the 10-m wind speed relative to the sea surface under neu-
 142 tral conditions (Edson et al., 2013, Appendix) and coefficients $m = 0.0017$ and $b =$
 143 -0.005 (Edson et al., 2014). Hereafter, U_{r10N} is defined such as:

$$U_{r10N} = \frac{u_*}{\kappa} \ln(10/z_0), \quad (7)$$

144 The coefficients m , and b in Eq. 6, have been determined to fit the average
 145 data used in COARE3.5 over wind speeds between 5 and 18 ms^{-1} . If wind speed
 146 is below 5 ms^{-1} , the surface roughness is mainly determined by z_{smooth} in Eq. 4.
 147 For wind speeds greater than 18 ms^{-1} , COARE3.5 fixes the value of the Charnock
 148 coefficient to its value at 18 ms^{-1} . Note, however, that although α_{CH} is fixed above
 149 18 ms^{-1} , z_0^{rough} , C_D and τ all continue to increase with the wind speed, just at a
 150 lower rate.

151 An alternative way to define z_0^{rough} in COARE3.5 is to use the so-called wave-
 152 based formulation (WBF), which requires contemporary information about the wave
 153 field and its state of development, such as significant wave height (H_s) and phase
 154 speed of the dominant waves (c_p). Two WBFs are currently available in COARE3.5,
 155 one that uses the wave age only and another that uses both the wave age and wave
 156 steepness. In the second form, which is explored in this study in great detail, z_0^{rough}
 157 is expressed as

$$z_0^{rough} = H_s D \left(\frac{u_*}{c_p} \right)^B, \quad (8)$$

158 where u_*/c_p is the inverse wave age based on the friction velocity, and D and
 159 B are numerical constants given by $D = 0.09$ and $B = 2$ in Edson et al. (2013).
 160 Hereafter, we will use a definition of wave age based on the ratio of the phase speed
 161 of the waves at the spectral peak over the surface wind speed at 10 m defined as

$$\chi = \frac{c_p}{U_{10}}. \quad (9)$$

162 The wave age is used to describe the state of development of the wave field.
 163 For example, a wave age close to 1.2 represents a fully developed sea when the sur-
 164 face waves and stress are largely in equilibrium (e.g., Phillips, 1985), in which the
 165 rate that wind does work on the surface waves is balanced by the dissipation rate of
 166 breaking waves (microbreakers and whitecaps) and nonlinear wave-wave interactions
 167 (e.g., Csanady & Gibson, 2001). Wave ages under 1 are associated with developing
 168 seas and young waves, while wave ages well above 1.2 describe decaying seas and
 169 swell. It should be noted that in the current COARE3.5, c_p is defined using the peak
 170 period of the waves, T_p , in deep water such that:

$$c_p = g \frac{T_p}{2\pi}. \quad (10)$$

171 In Section 3, we will examine the sensitivity of the estimated momentum flux
 172 based on the current COARE3.5 algorithm. Guided by comparison to the observa-
 173 tions in Section 4, we will then explore the impacts of revised COARE3.5 WBF in
 174 Section 5.

175 2.2 SCOAR regional coupled model system

176 We use the Scripps Coupled Ocean-Atmosphere Regional (SCOAR) model
 177 (Seo et al., 2007, 2021), which couples the Weather Research and Forecast (WRF,
 178 Skamarock et al., 2008) Model to the Regional Ocean Modeling System (ROMS,
 179 Shchepetkin & McWilliams, 2005) via the COARE3.5 bulk flux algorithm (Fairall
 180 et al., 1996, 2003; Edson et al., 2013). In the absence of wave coupling, ROMS
 181 is driven by the surface heat flux (Q_{NET}), momentum flux (τ), and freshwater
 182 flux (Q_{FW}) computed from the wind speed-only formulation in COARE3.5 imple-
 183 mented in WRF. In turn, ROMS inputs SST and surface current vectors (U_s) to the
 184 COARE3.5 to compute the surface fluxes (Figure 2).

185 2.3 Wave coupling in SCOAR

186 Taking advantage of the COARE's WBF, this study implemented the cou-
 187 pling of the third-generation spectral wave model WaveWatch-III (WW3 Tolman
 188 et al., 2002; The WAVEWATCH III Development Group, 2016) into the SCOAR.
 189 The centerpiece of the model coupling is the COARE3.5 implemented in the surface
 190 layer scheme in WRF to compute the air-sea fluxes. In this study, we use the Mellor-
 191 Yamada-Nakanishi-Niino (MYNN) surface layer scheme (Nakanishi & Niino, 2009;
 192 Jiménez et al., 2012), which over the ocean grid points computes the surface fluxes
 193 using the COARE3.5 WBF. WW3 is forced by the surface wind (U_{10}) from WRF
 194 and ocean current (U_s) from ROMS. WW3 then returns the significant wave height
 195 (H_s) and the phase speed of the dominant waves (c_p) determined based on T_p (Eq.
 196 10) to the MYNN surface layer scheme. In lieu of c_p , WW3 can alternatively send
 197 the mean phase speed (c_m) and peak wave direction (Section 5). Spatially varying
 198 Charnock coefficients (α_{CH}) are then updated to parameterize the surface roughness
 199 length (z_0) as a function of dominant wave age (χ) and wave steepness (Eq. 8). For
 200 this to work in WRF, the MYNN surface layer scheme has been modified to allow
 201 ingestion of wave age and significant wave height (H_s) from WW3. The MYNN PBL
 202 scheme (Nakanishi & Niino, 2004, 2006) is coupled to this modified surface layer
 203 scheme, allowing for the adjusted z_0 , wind stress (τ), and latent (Q_{LH}) and sensi-
 204 ble (Q_{SH}) heat fluxes to influence the kinematic and thermodynamics processes in
 205 the PBL. The surface layer scheme has also been modified to take the ocean sur-
 206 face currents (U_s) from ROMS to compute the relative wind and thus represent
 207 wind-current interaction. This so-called relative wind effect is represented in all
 208 simulations analyzed here.

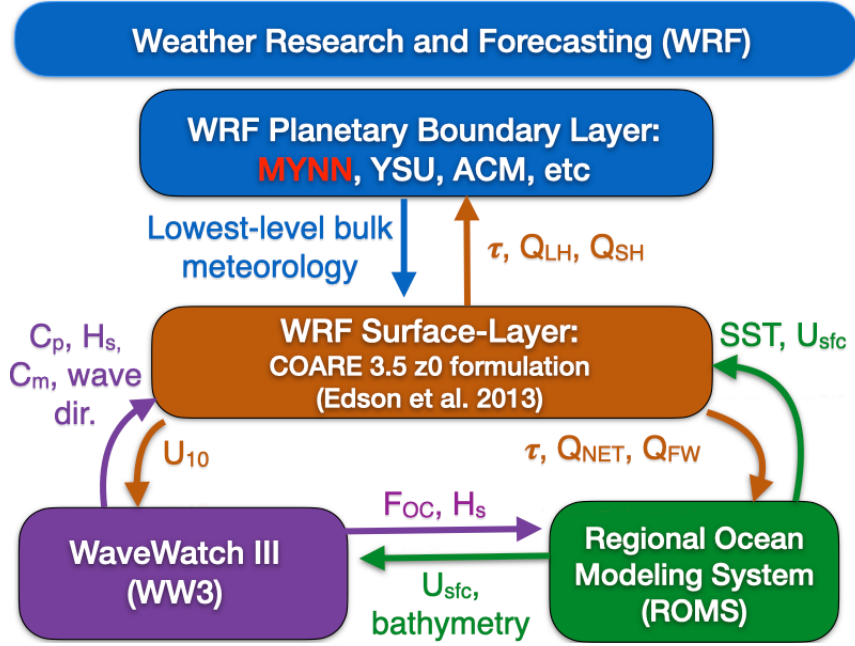


Figure 2. SCOAR WRF-ROMS-WW3 coupling flowchart. See the text for the variable names that are exchanged across the model components.

209

2.4 Experiments

210

211

212

213

214

215

216

217

218

219

220

221

222

223

224

In WRF, the deep cumulus convection is represented through the Multi-scale Kain-Fritsch scheme (Zheng et al., 2016), the cloud micro-physics by the WRF single-moment 6-class scheme (Hong & Lim, 2006). The Goddard radiation scheme (Chou & Suarez, 1999) is used for shortwave and longwave radiation. The land surface process is treated with the Noah land surface model (F. Chen & Dudhia, 2001). In ROMS, the KPP (K profile parameterization) scheme (Large et al., 1994) determines vertical eddy viscosity and diffusivity. The vertical grid in ROMS is stretched to enhance the resolutions near the surface and the bottom, using the so-called stretching parameters of $\theta_s = 7.0$, $\theta_b = 2.0$, and $h_{cline} = 300$ m. In WW3, the set of parameterizations from Ardhuin et al. (2010) is used, including swell dissipation scheme (Ardhuin et al., 2009). Nonlinear wave-wave interactions are computed using the discrete interaction approximation (Hasselmann et al., 1985). Reflection by shorelines are enabled through Ardhuin and Roland (2012) scheme. The depth-induced breaking is based on Battjes and Janssen (1978), and the bottom friction formulation follows Ardhuin et al. (2003).

225

226

227

228

229

230

The model domain covers the Northwest Tropical Atlantic Ocean (Figure 3). The horizontal resolutions in WRF, ROMS, and WW3 are identical 10 km, with matching grids and land-sea masks. ROMS (WRF) is run with a stretched vertical grid with a total of 30 (33) vertical levels, with approximately 10 layers in the upper 150 m (below 1300 m). The model coupling is activated every 3 hours to account for the diurnal cycle.

231

232

233

234

235

A set of coupled model simulations presented in Section 4 is run for 6 months (November 1, 2019 to May 1, 2020), covering the ATOMIC/EUREC⁴A period, with a specific aim to compare with the measurements. In these simulations, the WRF model is initialized and driven by 3-hourly ERA5 global reanalysis at 0.25° resolution (Hersbach et al., 2018a, 2018b), ROMS by the daily MERCATOR International

236 global reanalysis at $1/12^\circ$ resolution (Lellouche et al., 2018), and WW3 by seven
 237 spectral points obtained from the global $1/2^\circ$ resolution WW3 simulations (Raschle
 238 & Ardhuin, 2013). The initial conditions for ROMS and WW3 were obtained from
 239 the respective ROMS-only and WW3-only spin-up simulations forced by ERA5 at-
 240 mospheric forcing (starting from January 1, 2019). In ROMS, the tidal forcing is
 241 obtained using the Oregon State University Tidal Prediction Software (Egbert &
 242 Erofeeva, 2002) and applied as a 2-D open boundary condition by prescribing the
 243 tidal period, elevation amplitude, current phase angle, current inclination angle, the
 244 minimum and maximum tidal current, and ellipse semi-minor axes for 13 major tidal
 245 constituents. Daily climatology estimates of the Amazon and River and Orinoco
 246 River discharges are obtained from the Observatory Service SO-HyBAM database
 247 (<https://hybam.obs-mip.fr/>), which are prescribed as point sources close to the river
 248 mouths in our grid.

249 The second set of simulations presented in Section 3 is identical to that of the
 250 6-month-long simulations, except that WRF, ROMS, and WW3 are initialized from
 251 respectively 3-hourly ERA5 global reanalysis for the atmosphere and ROMS-only
 252 and WW3-only spin-up simulations for the ocean and waves as described above
 253 and run on a particular day (January 8, 2020) as a case study investigation. The
 254 motivation for the short simulations with the identical initial condition is to isolate
 255 the immediate impacts on z_0 and τ before the coupled feedback begins to alter the
 256 state variables. One could use the identical input state variables to estimate the
 257 air-sea fluxes offline using different COARE formulations. This yields similar results
 258 (not shown), indicating that the difference we show in Section 3 is not due to the
 259 difference in state variables but due to the formulation difference. One notable ad-
 260 vantage to use the fully coupled model simulation is that it allows for evaluating the
 261 wind response beyond the surface layer (e.g., Figure 6c), and potentially large-scale
 262 feedback effects via the coupling.

Table 1. Summary of the different SCOAR experiments.

Experiments	z_0 parameterization	Relative wind	Wave period	misaligned wave
WSDF	wind speed [Eq. 5]	yes	/	/
WBF	wave age + wave steepness [Eq. 8]	yes	T_p	no
WBF $_{\theta}$	wave age + wave steepness [Eq. 11]	yes	T_p	yes
WBF $_{T_m}$	wave age + wave steepness [Eq. 12]	yes	T_m	no

263 Table 1 summarizes 4 experiments conducted in this study, where the only
 264 difference is in the way z_0 is parameterized in COARE3.5. In the first run (dubbed
 265 WSDF), the wind speed only formulation is used (hence, only WRF-ROMS cou-
 266 pling), while in the second run (WBF), the default wave-based formulation is used
 267 (WRF-ROMS-WW3). These two runs are examined in detail in Sections 3-4. Two
 268 additional runs, discussed in Section 5, are conducted with a modified wave-based
 269 formulation. WBF $_{\theta}$ takes into account the directional misalignment between wind
 270 and wave, while WBF $_{T_m}$ modifies the definition of wave age based on mean wave
 271 period rather than the peak wave period.

272 All simulations used in this study produce output every 3h. Since this output
 273 interval is much coarser than the typical sampling intervals used in the observations
 274 (Section 2e), there is inevitable inconsistency in sampling frequency and the number
 275 of samples between the model and data. We attempt to increase the model sample
 276 size and capture more spatio-temporal variability by sampling a slightly broader

277 region of the model domain encompassing the particular observational tracks (gray
 278 areas in Figure 1a).

279 **2.5 ATOMIC/EUREC⁴A observations**

280 This study will exploit direct and indirect measurements of momentum
 281 fluxes and relevant wave fields from various platforms deployed during the
 282 ATOMIC/EUREC⁴A experiment. Figure 1 shows the tracks of the different obser-
 283 vational platforms, including the R/V Ronald H. Brown (RHB, Quinn et al., 2021;
 284 Thompson et al., 2021), R/V ATALANTE (Bourras, Geyskens, et al., 2020), SWIFT
 285 drifters (Surface Wave Instrument Float with Tracking, Thomson, 2012; Thomson
 286 et al., 2019, 2021), and OCARINA (Ocean Coupled to Atmosphere, Research at
 287 the Interface with a Novel Autonomous platform, (Bourras, Branger, et al., 2020)
 288 surface naval drone. The RHB provides direct momentum flux measurements every
 289 10 minutes in the so-called “Tradewind Alley” region from January 9 to February
 290 13, 2020. The SWIFT drifters were deployed from the RHB, from which the hourly
 291 stress can be estimated using the equilibrium frequency range in the wave spectrum
 292 (Iyer et al., 2021). The R/V ATALANTE measured the wind stress mostly in the
 293 “Eddy Boulevard” region based on the inertial dissipation method. OCARINA was
 294 deployed from the R/V ATALANTE from January 25 to February 17, 2020 (with
 295 some discontinuity), providing direct wind stress measurements every minute.

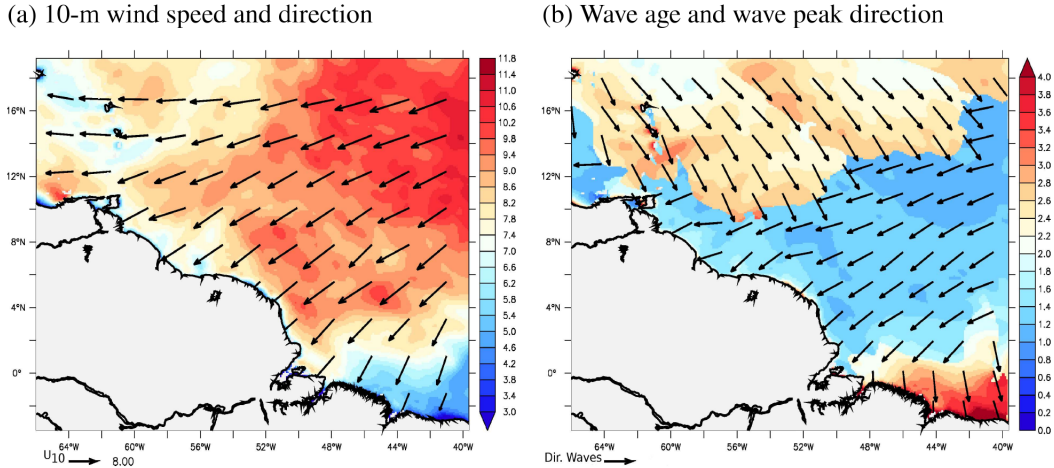


Figure 3. Snapshots of (a) 10-m wind speeds (shading) and direction (arrows) and (b) peak wave age (shading) and wave peak direction (arrows) on January 8, 2020 at 0600 UTC.

296 **3 Impacts of wave and sea state: a case study**

297 To demonstrate the immediate effect of including waves on z_0 and τ in the
 298 COARE3.5 using a coupled model, we will first compare the simulation results close
 299 to the initial condition. By doing so, the input state variables into the bulk formula
 300 remain largely identical, and any differences in simulated z_0 and τ can be attributed
 301 to the difference in the formulations. From this set of experiments, we will compare
 302 the results 3 hours after the initial condition.

303 The sea state and wind fields on January 8, 2020 at 0600 UTC, shown in Fig-
 304 ure 3a, illustrate the archetypal synoptic condition observed in this region during the
 305 boreal winter. Much of the domain was under the influence of northeasterly trade

306 winds with wind speeds of $7\text{-}13\text{ ms}^{-1}$, while the northern and southeastern parts of
 307 the domain experienced much weaker ($<7\text{ ms}^{-1}$) easterly and northerly winds, re-
 308 spectively. Figure 3b shows the corresponding wave age and peak wave direction. In
 309 the Tradewind Alley region, surface waves were predominantly downwind with rela-
 310 tively small wave age, indicating the developing seas with young waves. Away from
 311 the trade winds, especially in the northern part of the domain, the wave vectors are
 312 generally misaligned with the local wind vectors, and the wave age is high, indicative
 313 of the swell-dominated sea state.

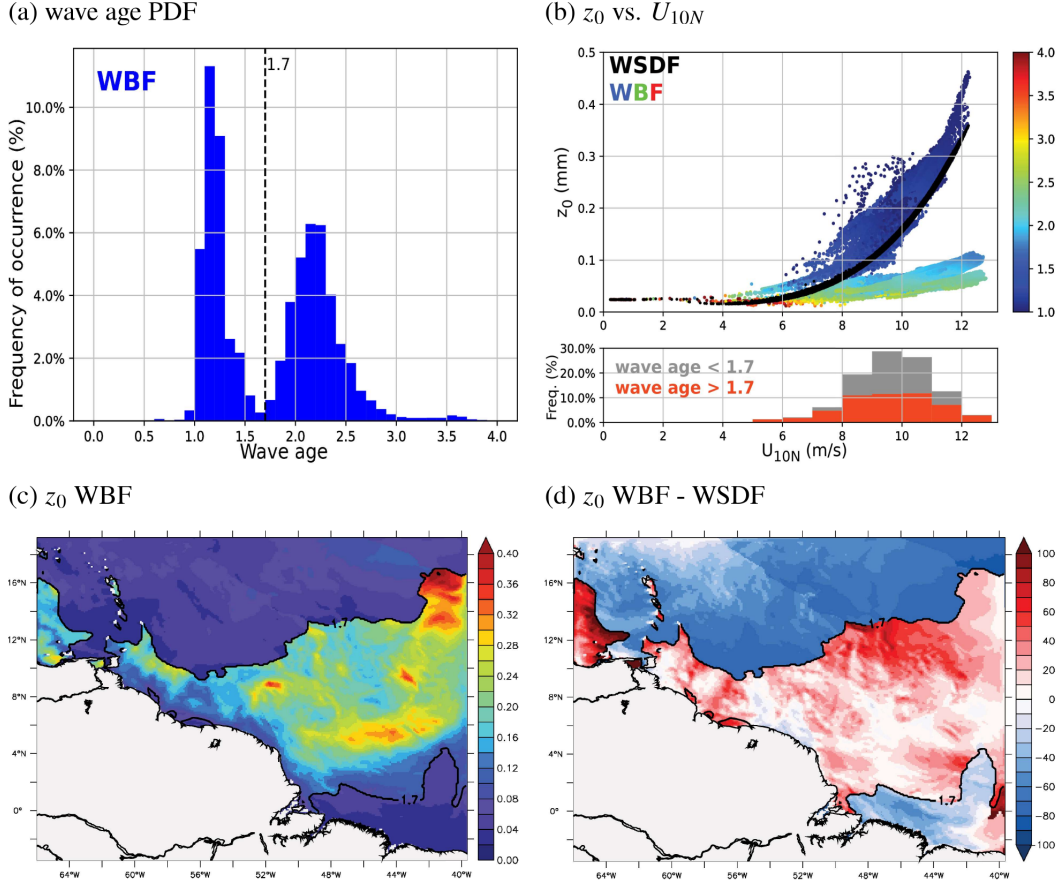


Figure 4. (a) PDF of wave age from the entire model domain on January 8, 2020 at 0600 UTC. The dotted vertical line denotes the wave age of 1.7, below (above) which the sea state is characterized as developing, equilibrium and slightly old waves (mature waves and swell). The upper panel of (b) is a scatter plot of z_0 (mm) vs. U_{10N} (ms^{-1}). z_0 from WSDF is shown in black, while z_0 from WBF is color-coded to denote the corresponding wave age. The stacked PDFs of U_{10N} in the lower panel of (b) are constructed when wave age is above 1.7 (red) and below 1.7 (gray). (c) A map of z_0 from WBF, superposed with a contour of wave age = 1.7. (d) A map of percentage difference of z_0 between WBF and WSDF

314 To illustrate sea state distribution differently, Figure 4a shows the probabil-
 315 ity density function (PDF) of wave age for the same period. Two distinct peaks of
 316 wave age stand out clearly. The first peak resides on wave age between 0.8 and 1.7,
 317 corresponding to developing (young) waves to fully developed (mature) seas. The
 318 secondary peak is found over a wide range of wave age greater than 1.7, reaching
 319 up to 4-5, the latter representing swell. Indeed, the fact that there is a gap at 1.7

320 strongly suggests that the older waves are swell, as opposed to the continuum of
 321 longer/older wind waves. Thus, in this case, we choose to use 1.7 as a threshold for
 322 fully developed seas and not the usual value of 1.2 which is what you might expect
 323 for wind waves dominated region. As a matter of fact, this swell-dominated sea state
 324 is frequently observed in the ATOMIC region in the boreal winter (e.g., Semedo et
 325 al., 2011; Jiang & Chen, 2013). Indeed, if considering the entire month of January
 326 2020 in our simulations, we find that wave ages greater than 2 occur more than 60%
 327 of the time in this domain.

328 Figure 4b compares the z_0 against wind speed from the WSDF (black) and
 329 WBF (color) runs for this period. z_0 from WBF is color-coded to denote the cor-
 330 responding wave age. The bottom panel shows stacked PDFs of 10-m wind speeds
 331 from WBF, with the red (gray) parts representing the proportion of wind associ-
 332 ated with wave age over (under) 1.7. The WSDF in COARE3.5 assumes young seas
 333 under moderate to high winds, and hence the parameterized z_0 (black) obeys the
 334 well-known quadratic dependence on wind speed. The surface roughness z_0 from
 335 WSDF shows less scatter because it is based solely on wind speed.

336 In contrast, WBF captures the two wave age-dependent regimes of z_0 that ap-
 337 pear distinct from WSDF. The first is the cluster of z_0 , which increases more rapidly
 338 with wind speed than WSDF z_0 and occurs over $4\text{--}12\text{ ms}^{-1}$. The wave age of this
 339 cluster (shading) is typically less than 1.7, corresponding to the first wave age peak
 340 in Figure 4a of small-scale young waves. Thus, the developing and equilibrium waves
 341 under these wind speeds and wave age conditions increase z_0 in WBF compared to
 342 WSDF.

343 The second cluster indicates significantly decreased z_0 in WBF with wind
 344 speed up to 12 ms^{-1} . This cluster can be further split into two different wind speed
 345 groups, under and above 8 ms^{-1} , color-coded by the PDF of winds (Figure 4b).
 346 Below 8 ms^{-1} (red, weak winds), the wave age tends to be greater than 1.7, where
 347 remotely generated swell appears to dominate the sea state. However, the wind
 348 speeds under 8 ms^{-1} account for less than 10% of the total wind speed data, and
 349 thereby it has a relatively small impact on the space/time-averaged z_0 . Indeed,
 350 when averaged for wind speed below 8 ms^{-1} , the percentage difference in z_0 between
 351 WSDF and WBF, defined as $(\text{WBF-WSDF}/\text{WSDF}) * 100$, is only -1.7%.

352 During this day, most of the wind speed is above 8 ms^{-1} . In addition to the
 353 proportion of low wave age expected under this moderately high wind speed, we
 354 also find an increased occurrence of large wave age, accounting for about 50% of
 355 the data (Figure 4b). The co-existence of high wind and swell indicates a mixed
 356 sea condition. In this case, when averaged over wind speed above 8 ms^{-1} , the swell
 357 impact appears much more significant, with z_0 in WBF being 15.7% lower than
 358 that in WSDF. The working hypothesis is that the use of the phase speed at the
 359 spectral peak causes the WBF to assume that the swell is supporting most of the
 360 stress; even under moderate winds. The strong impact of swell at moderate winds is
 361 questionable and will be a focus of this investigation.

362 The spatial distribution of z_0 from WBF is shown in Figure 4c. The z_0 dif-
 363 ference between WBF and WSDF is shown in Figure 4d. As in Figure 4a,b, two
 364 distinct regimes of z_0 are readily apparent on the map, delineated sharply by the
 365 contour of wave age 1.7 (black). In the first regime of increased z_0 in WBF under
 366 moderate to strong trade winds, the WBF predicts an increased z_0 by on average
 367 $\approx 50\%$ compared to WSDF. This increased z_0 is expected as the WBF z_0 formula-
 368 tion (Eq. 8) takes into account the effect of wave slope on the aerodynamic rough-
 369 ness of the sea surface. That is, Figure 5a,b show that wave slope under young
 370 waves is higher, where the choppy sea surface increases z_0 . Figure 5c,d shows the
 371 angle (θ) between the wind direction and peak wave direction. If $\theta = 0^\circ$, wind and

372 waves are perfectly aligned, whereas $\theta = 180^\circ$ means wind and waves are opposed.
 373 Under this wind/wave regime, the peak wave direction is largely downwind since θ is
 374 generally less than 50° . This corroborates that these waves are young waves driven
 375 by local winds.

376 Figure 4d also shows the second regime of decreased z_0 with the inclusion of
 377 waves, especially in the northern part of the domain. In this region, the remotely
 378 generated swell propagates into the domain through the northern boundary and
 379 forms a sea state with the aerodynamically smooth sea surfaces (Figure 5a,b) and
 380 with waves whose direction is strongly misaligned ($\theta = 60-160^\circ$) with the local wind
 381 (Figure 5c,d). In particular, the reduced z_0 over swell persists under wind speed of
 382 up to 12 m s^{-1} (Figure 3a), despite the expectation that under such a high wind, the
 383 wind-waves would still strongly increase the aerodynamic roughness and stress.

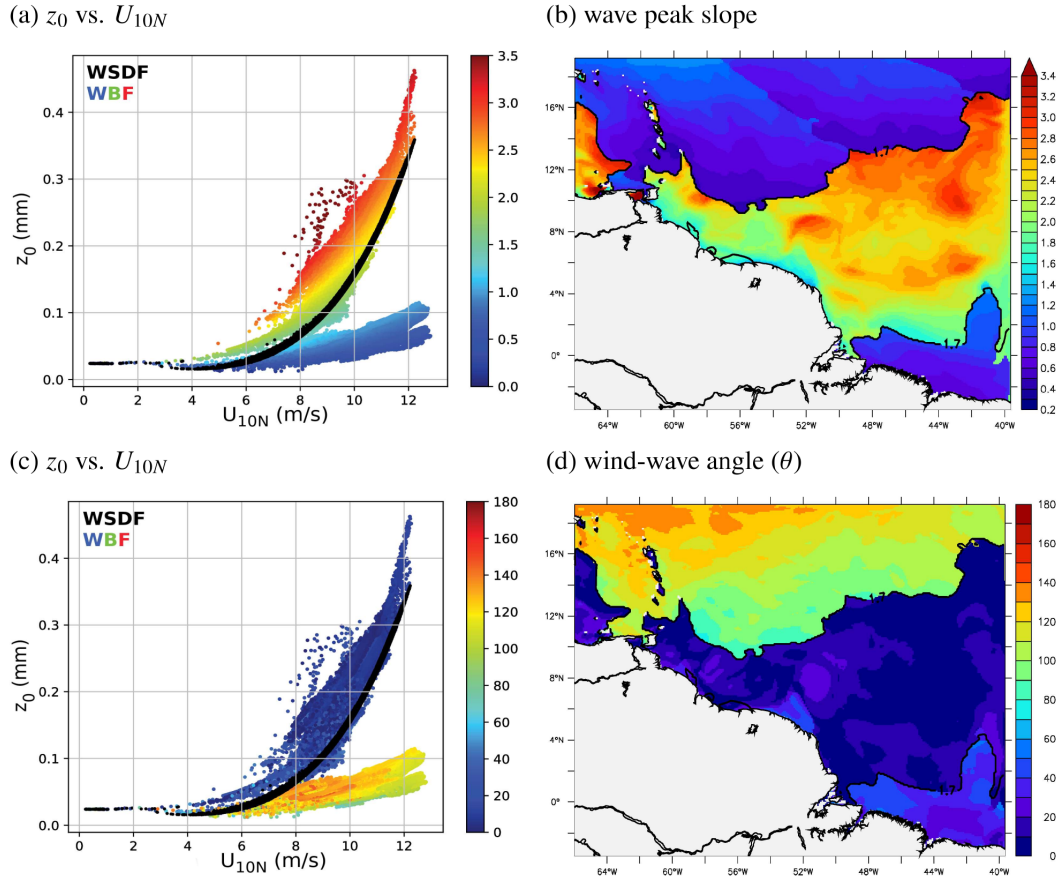


Figure 5. (a) Scatter plot of z_0 (mm) vs. U_{10N} (m s^{-1}) from WSDF in black and WBF color-coded to denote the corresponding wave peak slope (10^{-2}) defined as H_s/L_p where L_p is the peak wavelength. (b) A map of wave slope peak (10^{-2}), superposed with a contour of wave age = 1.7 on January 8, 2020 at 0600 UTC. (c,d) As in (a-b) except that colored scatters and shading denote the angle between the wind and wave directions ($^\circ$).

384 Figure 6a,b compare the parameterized wind stress in WBF and WSDF. One
 385 can see from these plots a consistent difference in wind stress due to the inclusion of
 386 waves. Wind stress decreases sharply in wind speeds of $8-12 \text{ m s}^{-1}$ over the northerly
 387 swell where wave age >1.7 . The percentage difference in wind stress magnitude
 388 exceeds 10%. Conversely, wind stress is increased in WBF by $\approx 4\%$ over fully devel-

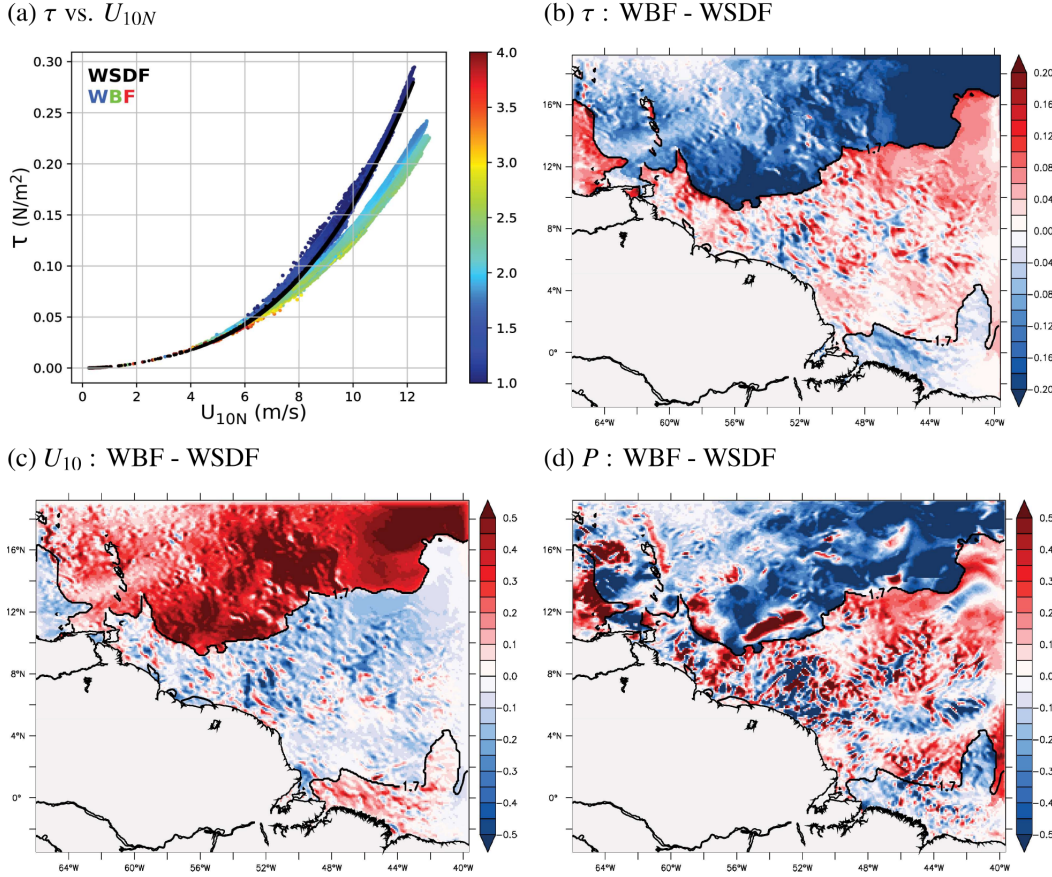


Figure 6. (a) Scatter plot of τ (Nm^{-2}) vs. U_{10N} (ms^{-1}) from WSDF in black and WBF color-coded to denote the corresponding wave age. (b,c,d) Difference maps between WBF and WSDF of (b) τ ($10^{-1} Nm^{-2}$), (c) U_{10} (ms^{-1}), and (d) wind work (P , $10^{-5} m^3 s^{-3}$) on January 8, 2020 at 0600 UTC, superposed with a contour of wave age = 1.7.

389 opened seas (wave age < 1.7) and high winds, consistent with the increase in z_0 there
 390 (Figure 4c). By comparing to the direct momentum flux observations, we will deter-
 391 mine in Section 4 if such reduced z_0 and τ over swell conditions at moderate to high
 392 wind speeds are consistent with the observations. As COARE3.5 does not consider
 393 the misaligned waves with winds, these conditions may constitute a source of uncer-
 394 tainty in the parameterized z_0 and τ via COARE3.5 WBF. As for the large wave age
 395 in the southeastern corner of the domain, it is concurrent with weaker winds (Figure
 396 3a), and hence the assumptions about the swell under weaker wind seem valid in
 397 this region. This leads to a small difference in z_0 between WBF and WSDF.

398 The altered stress directly influences the low-level winds via the surface drag.
 399 Here, we estimate the response in low-level winds at the lowest WRF model layer,
 400 at about 27 m above the sea surface. Figure 6c shows that the low-level wind is
 401 increased over the aerodynamically smooth sea surface due to swell by $>0.5 ms^{-1}$,
 402 accounting for 5-20% of the wind speed in WBF. Although weaker than under swell
 403 conditions, in the Tradewind Alley, where the stress in WSDF was enhanced over
 404 the fully developed waves, the wind stress is increased by 5% and the wind speed is
 405 decreased.

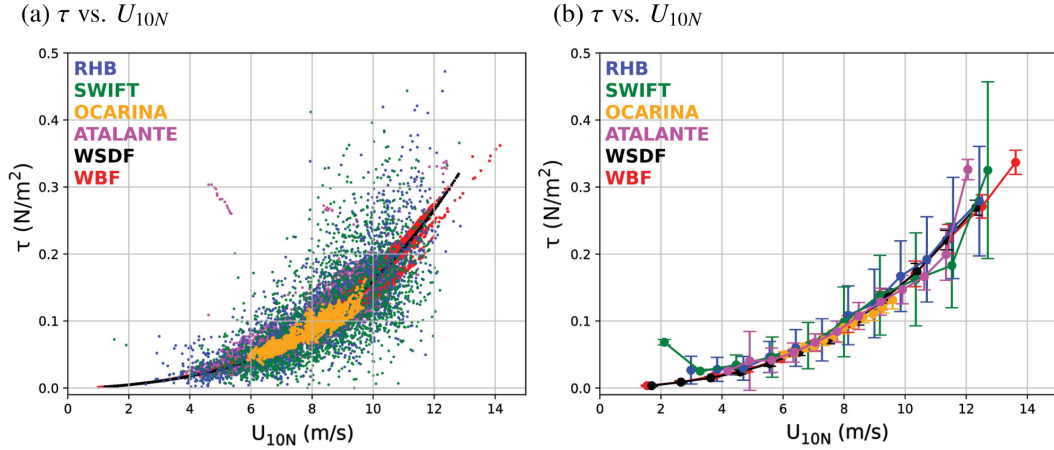


Figure 7. (a) Scatter plot comparing the two parameterized τ (Nm^{-2}) using COARE3.5 WSDF (black) and WBF (red) against the various types of measurements of τ (see Section 2e for a description of the various methodologies). (b) As in (a) except that measurements are bin-averaged with a wind speed bin-size of $U_{10N} = 1 \text{ ms}^{-1}$. The error bars represent ± 1 standard deviation.

406 One relevant physical process that represents the air-sea momentum transfer
 407 affecting the winds and surface currents, is the wind work (P),

$$P = \frac{1}{\rho_o} (\overline{u_s \tau_x} + \overline{v_s \tau_y}), \quad (11)$$

408 where (u_s, v_s) are the surface current vectors, (τ_x, τ_y) are the wind stress vec-
 409 tors, and the overbar denotes the time-average. When P is positive, the mechanical
 410 work is done by the wind stress on the ocean surface currents, increasing the ocean
 411 kinetic energy (e.g., Wunsch, 1998). When negative, it represents the diversion of
 412 the ocean energy by the current to the wind, accelerating the low-level winds at
 413 the expense of weakened surface currents (e.g., Renault et al., 2016, 2017; Seo et
 414 al., 2019, 2021). Figure 6d shows the difference in P between WBF and WSDF for
 415 this snapshot. The region of reduced τ and increased low-level wind in the swell-
 416 dominated region is congruent with the region of the robust decrease in P , while the
 417 opposite is true in the Tradewind Alley region. The difference in P mainly reflects
 418 the changes in wind stress due to waves (Figure 6b).

419 4 Modeled and observed momentum fluxes during ATOMIC

420 Determining whether or not the parameterized z_0 and τ with WBF represents
 421 an improvement over WSDF requires a detailed comparison to direct covariance
 422 stress measurements. In this section, we will compare the model simulation with
 423 the observations during the EUREC⁴A/ATOMIC experiments to evaluate the accu-
 424 racy of the wave-based parameterized τ and identify the regimes where further
 425 improvements might be needed.

426 Figure 7a compares the two modeled stresses to the observations. All observa-
 427 tions and the two model simulations display the quadratic relationship of wind stress
 428 with wind speed. RHB and SWIFT, sampling the stress mainly in the Tradewind
 429 Alley region, produce greater scatter compared to ATALANTE and OCARINA,
 430 which were deployed further south in the Eddy Boulevard region (1a). The signifi-

431 cant departure from this curve in the Tradewind Alley region may reflect the greater
 432 uncertainties in determining τ from these measurements. Between the model simulations,
 433 WBF produces a larger spread than WSDF, yet their averages at given wind
 434 speed are similar (Figure 7b). Overall, parameterized stresses by WSDF and WBF
 435 both agree well with the observations to within the observational errors during the
 436 campaign.

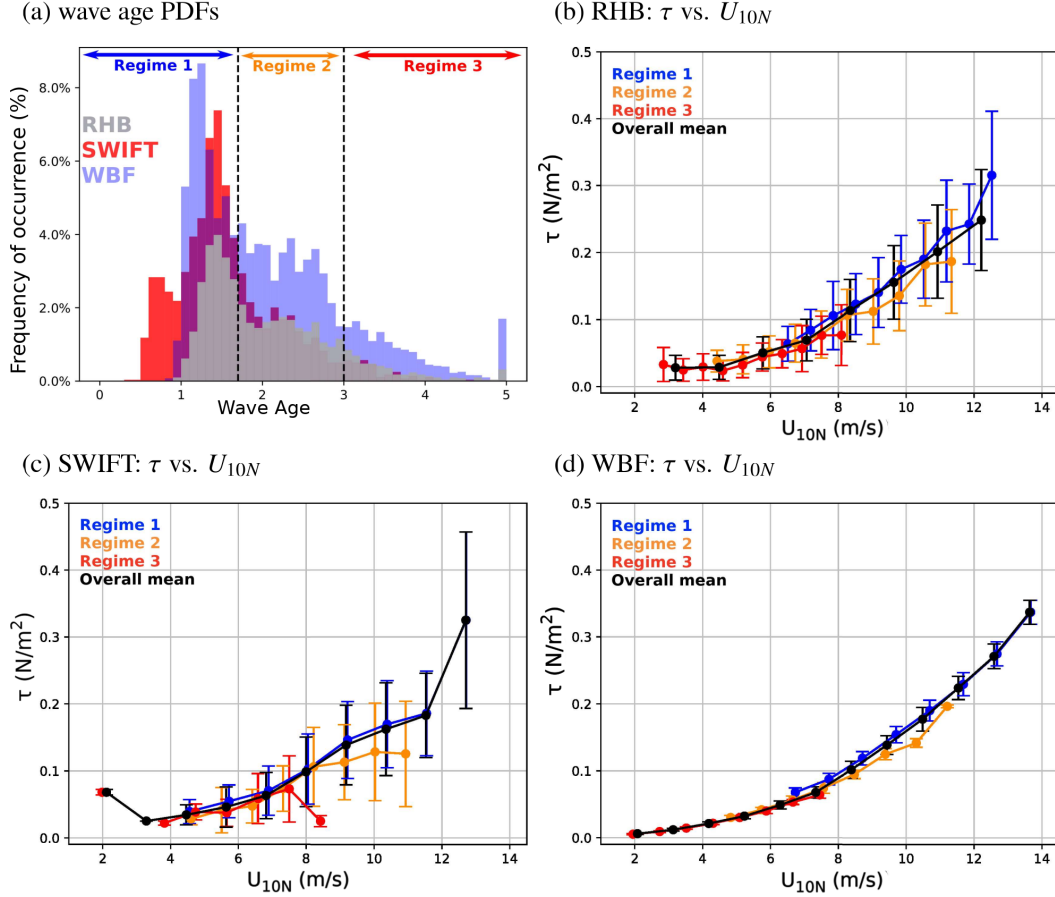


Figure 8. (a) Peak wave age distribution estimated from SWIFT (red), RHB (gray), and WBF (blue). Here, wave age is capped at 5. Three wave age regimes are defined: Regime 1 (blue) when wave age < 1.7 denotes the young sea to fully developed sea, Regime 2 (orange) when wave age is between 1.7 and 3 indicates the mature to old sea, and Regime 3 (red) when wave age > 3 represents the old sea and non-locally generated swell. (b-c) Binned scatter plots of τ (Nm⁻²) vs. U_{10N} (ms⁻¹), color-coded to show the three different wave age Regimes, with the bin-average of 1 ms⁻¹. The mean of all wave ages is shown in black. (d) As in (b) and (c) except from the WBF run. Here WBF is sampled along-track of the RHB and SWIFT.

437 Figure 8a compares the histograms of the wave age from the WBF run to those
 438 from the SWIFT drifters and the RHB. It should be noted that in both the model
 439 and measurements, the wave age is estimated using the peak period (T_p). The obser-
 440 vations and model simulation show the bi-modal distribution of wave age as was
 441 seen from the snapshot case in Section 3 (Figure 4a), with the first peak near wave
 442 age 1.7 and the secondary, much broader, peak between 2.5-3. The SWIFT obser-
 443 vations (in red) capture a higher occurrence of young waves than the RHB obser-

444 vations or the WBF simulation. WBF also features a fatter tail of the distribution
 445 toward larger wave ages, indicating that the model overemphasizes the occurrences
 446 of swell and decaying waves compared to these observed estimates.

447 Given the wave age distributions, we then divide the distribution into 3 dif-
 448 ferent “Regimes” to better understand the wave age-dependent z_0 -wind speed and
 449 τ -wind speed relationships. Regime 1 refers to young to fully developed seas, defined
 450 as when wave age < 1.7 , while Regime 2 indicates the mature to old sea, including
 451 mixed sea state, which is diagnosed as wave ages between 1.7 and 3. Finally, the old
 452 sea and non-locally generated swell characterizes Regime 3 estimated as when wave
 453 age > 3 . Note that these thresholds for different Regimes (e.g., the choice of peak
 454 wave age of 3) are not unique, but can vary depending on specific conditions and
 455 time periods under consideration.

456 The colored lines in Figures 8b and c show the bin-averaged surface stress
 457 from the RHB and the SWIFT from the 3 Regimes. The black lines denote the
 458 bin-averaged surface stress across all wave age regimes. Despite the significant error
 459 bars, which represent ± 1 standard deviation, one can observe the consistent rela-
 460 tionship between the measured stress and the wind speed across different wave age.
 461 For example, the measured stress over Regime 1 (blue) is higher than the overall
 462 average (black) as the short-wind waves support the bulk of momentum exchanges.
 463 In contrast, the stress over Regime 2 (orange) and Regime 3 (red) is lower than the
 464 overall average, as the sea state is characterized by mixed and older seas. This sea
 465 state dependence of wind stress is also somewhat evident in the WBF simulation
 466 (Figure 8d) despite the smaller error bars likely due to smaller number of samples in
 467 the model, as discussed in Section 2d.

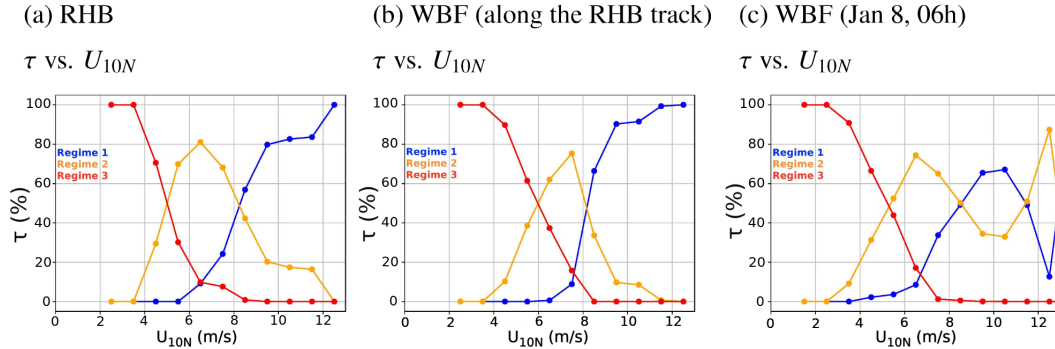
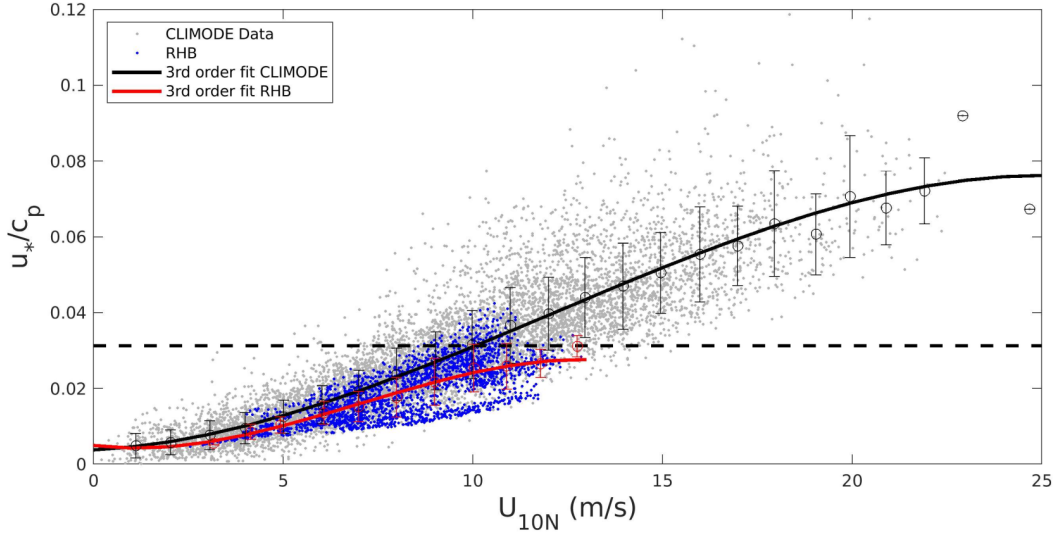


Figure 9. Percentage contribution of τ (%) by the three different wave age Regime at a given wind speed (bin averaged every 1 ms^{-1}) from (a) RHB, (b) WBF sampled along the RHB track between January 9 and February 13, 2020 and (c) WBF sampled over the whole model domain on January 8, 2020 at 0600 UTC. The different colors denote the different wave age categories described in Figure 8.

468 To further quantify this relationship, Figure 9a shows the percentage of stress
 469 supported by the different wave-age Regimes from the RHB observations, binned
 470 over 1 ms^{-1} intervals. Under 4 ms^{-1} wind speeds, the surface stress is mainly
 471 supported by Regime 3 (red), whereas above 8 ms^{-1} , Regime 1 (blue) dominates
 472 the contribution to the stress. Regime 2, which represents mixed sea conditions
 473 (orange), mainly supports the surface stress at low to moderate wind speeds (4-8
 474 ms^{-1}) and contributes to less than 20% of the stress above 10 ms^{-1} . Figure 9b
 475 shows the same diagnostics but for the WBF run sampled along the track of RHB.
 476 It shows that the WBF overall exhibits a similar fractional contribution to stress.

(a) u_*/c_p vs. U_{10N}



(b) u_*/c_p vs. U_{10N}

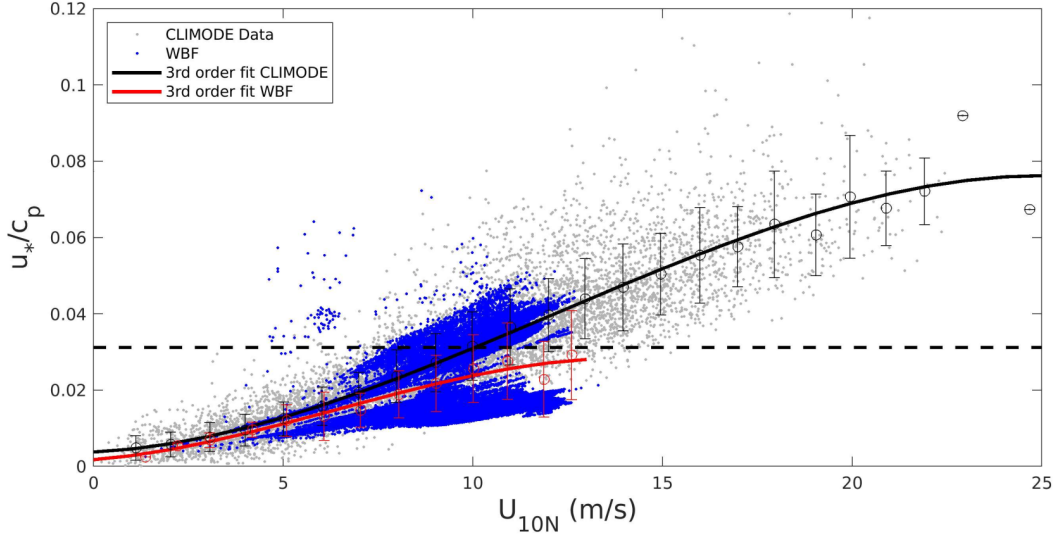


Figure 10. (a) Scatter plot of inverse peak wave age (u_*/c_p) vs. U_{10N} ($m s^{-1}$) for CLIMODE data (gray) and RHB data (a, blue). Bin-averages with the 1 standard deviation error bars are overlaid, at $1 m s^{-1}$ interval, along with the 3rd order fit (line) for CLIMODE (black) and RHB (red). The horizontal dashed line is $u_*/c_p = 0.03$, denoting the threshold for fully developed seas (equivalent to $c_p/U_{10N} = 1.2$). (b) As in (a) but RHB data is replaced with WBF on January 8, 2020 at 0600 UTC.

477 When the model is compared to the observations at this particular track and
 478 these time periods, WBF appears to accurately characterize the observed stress re-
 479 lationship with wave age (See also Figure 8). However, if sampled over a broader re-
 480 gion under a specific synoptic condition featuring strong swell and moderate winds,
 481 a quite different result is obtained. Figure 9c shows the same results as Figure 9b,
 482 except that the entire model domain is sampled under the same synoptic condi-
 483 tion examined in Section 3. In this case, the parameterized stress under moderately

484 strong 8-12 $m s^{-1}$ wind speeds supported by Regime 2 (orange) is comparable to the
 485 stress supported by Regime 1 (blue). This is different from the result from Figure
 486 9b but is consistent with the significantly reduced stress over wave age of 1.7-3 and
 487 wind speeds of 8-12 $m s^{-1}$ shown in Figure 6. This indicates that, because the RHB
 488 sampled mainly in the Tradewind Alley region, it did not capture other regions under
 489 the same synoptic condition where WBF assumes that the swell corresponding
 490 to the spectral peak support the lower wind stress despite the moderately strong
 491 wind speeds of 8-12 $m s^{-1}$. Since, in reality, short wind-waves under such wind
 492 speeds should still support the increased stress despite the higher wave age, we believe
 493 this is a form of deficiency in COARE3.5 WBF in representing the wind stress
 494 over mixed swell-dominated seas.

495 In fact, the COARE3.5's WBF was developed and tuned primarily by using
 496 the wave data collected from the extratropics, where sea state tends to be dominated
 497 by growing and fully-developed waves under high winds (see Figure 2 in Edson et
 498 al., 2013). Figure 10 compares the sea state used to tune COARE3.5, taken during
 499 the CLIMODE campaign (CLIVAR Mode Water Dynamic Experiment, Marshall et
 500 al., 2009), with the sea state observed by RHB during January-February 2020 and
 501 modeled in WBF on January 8, 2020 at 0600 UTC in the ATOMIC region. It shows
 502 the relationship between the inverse wave age and U_{10N} . Here, a low inverse wave
 503 age is indicative of decaying seas and swells. An inverse wave age of 0.03 (dashed
 504 line) is roughly equivalent to an equilibrium wave age of 1.2. As expected, the sea
 505 state captured in the ATOMIC region is very different and much older than the
 506 one used in COARE3.5. Therefore the wind stress under moderate winds and swell
 507 dominated conditions observed here, and possibly in other tropical oceans, may not
 508 be currently well parameterized in the COARE3.5 WBF. The specific deficiency
 509 identified from this analysis is that, for mixed seas (Regime 2) where high wave age
 510 and moderately strong wind co-occur, the current COARE3.5 WBF overemphasizes
 511 the swell impact on wind stress, leading to the low-stress bias despite the moderately
 512 strong winds.

513 **5 The revised wave-based formulation in COARE3.5**

514 In the following, we present two experimental revisions to the z_0 formulation in
 515 the current COARE3.5 WBF for swell conditions coincident with moderate to high
 516 winds, the condition that is frequently observed in the northern ATOMIC region
 517 in the boreal winter. One method is to replace the peak wave period (T_p) with the
 518 mean wave period (T_m) in the definition of the phase speed and thus wave age, and
 519 another is to incorporate the effect of misaligned waves with local wind on aerody-
 520 namic roughness in the z_0 parameterization. In essence, these two observationally-
 521 guided approaches desensitize the impact of swell on z_0 and τ estimates at moderate
 522 winds and alleviate the low biases in the current COARE3.5 WBF. For this, we now
 523 return to the case study on January 8, 2020 as in Section 3.

524 **5.1 The mean wave period**

525 One possible approach to mitigate the overestimation of the swell impact on
 526 z_0 and τ under moderate to high winds is to use the wave's mean period, T_m , to
 527 calculate the average phase speed, c_m , in the wave age definition. This change is mo-
 528 tivated by the finding that T_p does not accurately describe a mixed-sea state where
 529 swell and wind-sea co-exist, as shown in Figure 10. T_p can be also sensitive to the
 530 spectral shape of the wave energy and the chosen filter, while T_m can be reliably es-
 531 timated from observations and WW3 as either an energy-weighted average period or
 532 zero-crossing period. A similar argument has been made recently by (Colosi et al.,

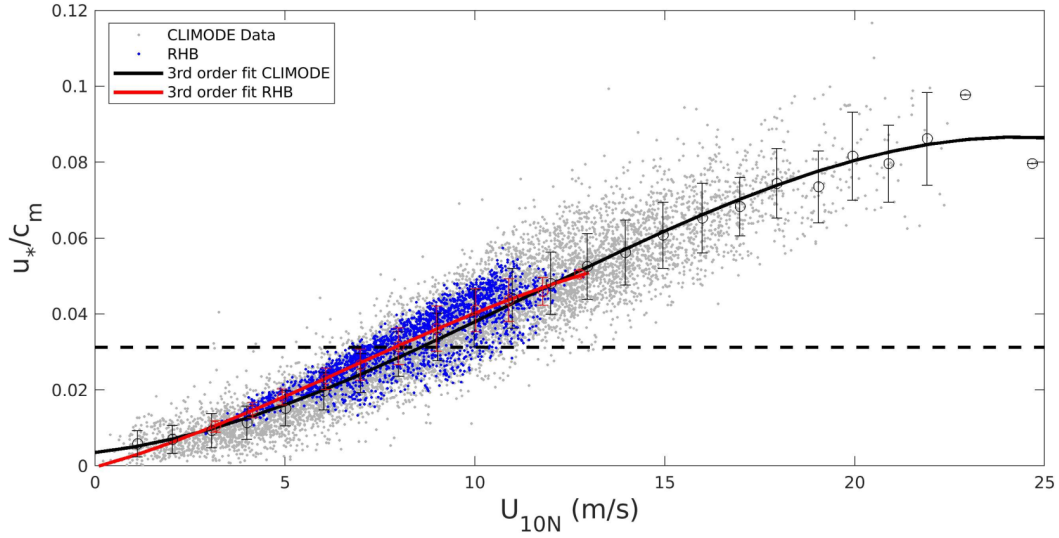
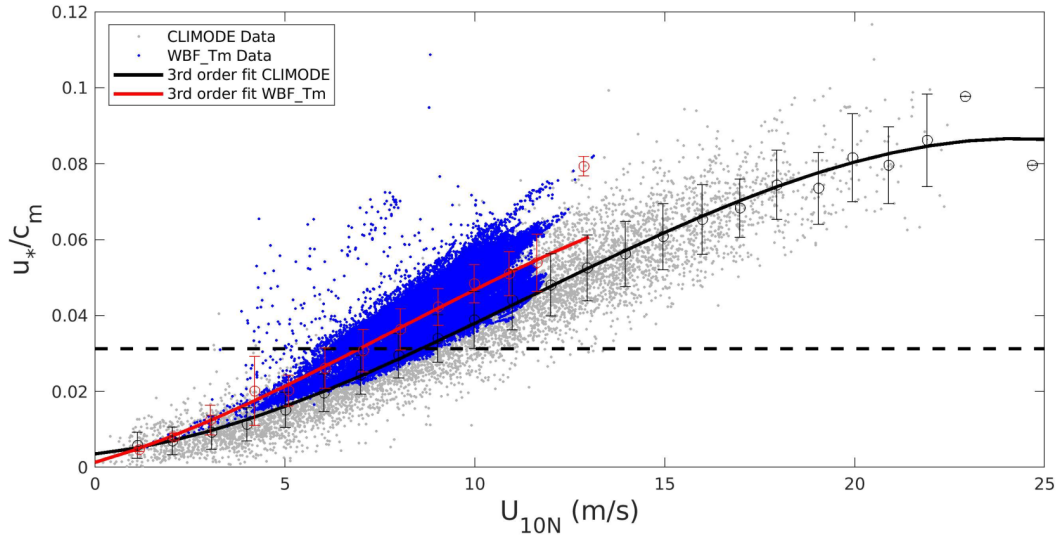
(a) u_*/c_m vs. U_{10N}

 (b) u_*/c_m vs. U_{10N}


Figure 11. (a) As in Figure 10a but with inverse mean wave age (u_*/c_m). The dashed line is $u_*/c_m = 0.03$, denoting the threshold for fully developed seas (equivalent to $c_m/U_{10N} = 1.2$). (b) As in Figure 10b except for showing the result from WBF T_m

533 2021) as they chose to use a wave age dependent computed with the mean period to
 534 construct the seasonal probability of swell over global oceans.

535 We carried out an additional coupled simulation, dubbed WBF T_m , where T_p
 536 is replaced with T_m to get the mean phase speed of the waves c_m in Eq. 12:

$$z_{rough} = H_s D \left(\frac{u_*}{c_m} \right)^B, \quad (12)$$

537 where $D=0.39$ and $B=2.6$, which have been tuned using the COARE3.5 set
 538 of observations. We will estimate T_m based on the zero-crossing period as it is the

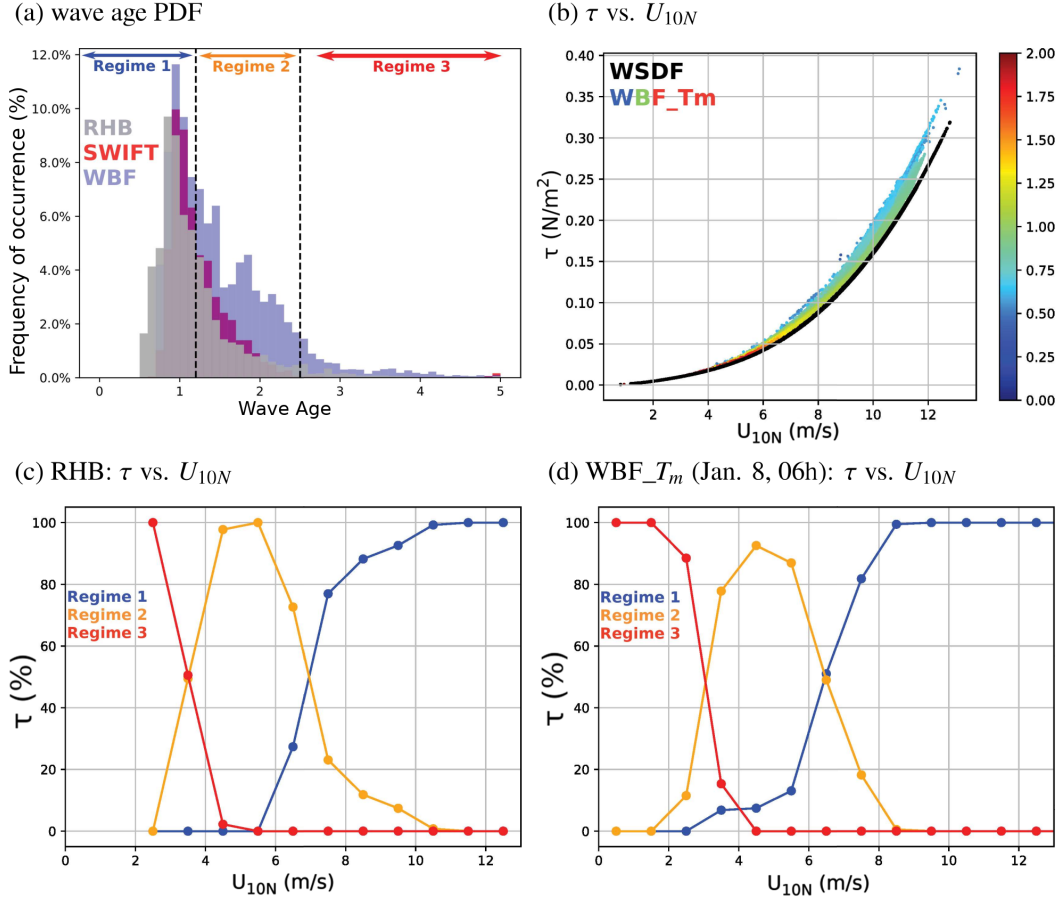


Figure 12. (a) Mean wave age distributions estimated from RHB (gray), SWIFT (red), and WBF T_m (blue). WBF T_m is sampled along-track of the RHB and SWIFT. (b) Scatter plot of τ (Nm^{-2}) vs. U_{10N} (ms^{-1}) from WSDF in black and WBF T_m color-coded to denote the corresponding wave age on January 8, 2020 at 0600 UTC. (c,d) As in Figure 9a,c, except that the wave age is defined with T_m for (c) RHB and (d) WBF T_m .

539 one used to describe T_m in the observation. Figure 11 shows the same diagnostics
 540 as in Figure 10 but this time using c_m to calculate the inverse wave age in both the
 541 observations, CLIMODE and RHB, and the WBF T_m run. The general trend of
 542 both sets of observations are now in good agreement (Fig. 11a). In WBF T_m , the
 543 use of c_m in eq. 12 alleviates the bias over the mixed sea (Regime 2) (Figure 10b vs.
 544 Fig. 11b) and shows a better agreement of the general trends from the observations.
 545 Further refinement of coefficients in eq. 12 will be addressed in more detail in the
 546 future release of the COARE4.0 algorithm.

547 Figure 12a shows the PDF of wave age for RHB (gray), SWIFT (red), and
 548 WBF T_m (blue) computed using T_m . This figure should be compared to Figure 8a
 549 where RHB, SWIFT and WBF wave age PDFs were computed using T_p . Similar to
 550 Figure 8a, wave age is capped at 5 to show the tail of the distribution. In contrast
 551 to the bi-modal distribution of wave age with the pronounced secondary peak of
 552 wave age estimate with T_p , the use of T_m effectively removes this secondary peak
 553 in both the model and observations, yielding a markedly different distribution with
 554 an overall prevalence of younger sea state. We adjusted the different categories of
 555 wave age defined previously to fit the new wave age distribution based on T_m . Fig-

556 ure 12b shows τ on January 8, 2020 at 0600 UTC from WBF_T_m , with wave age
 557 color-coded. The cluster of low z_0 with high wave age seen in Figure 4b is elimi-
 558 nated in WBF_T_m , because of the elevated z_0 and τ under moderate to high wind
 559 speeds. Finally, Figure 12c,d, to be compared to Figure 9a,c shows the percentage of
 560 τ supported by each category of wave age for RHB and for WBF_T_m , respectively.
 561 With the use of T_m , WBF_T_m agrees well with RHB concerning the fractional con-
 562 tribution from each sea state to the surface stress. Particularly over 7 m.s^{-1} , most of
 563 the contribution to τ now comes from the wind sea (blue), whereas the contribution
 564 of mature seas and swell subsides rapidly with the increased wind speeds. This is
 565 a clear improvement from τ parameterized using T_p (Figure 9c) and is much more
 566 consistent with the observations (Figures 9a, 12c).

567 5.2 Including the (mis)aligned wind-wave directions

568 As discussed in Section 2, the COARE3.5 assumes the wave stress as a scalar
 569 roughness parameter, and hence the direction of wave-stress vectors is aligned with
 570 the mean wind vectors. However, wave stress and mean wind vectors can be mis-
 571 aligned under various conditions, including under rapidly translating storms (e.g.,
 572 S. S. Chen et al., 2013), near strong vorticity and divergence gradients and density
 573 fronts (e.g., Villas Bôas & Young, 2020), or over mixed seas where wind waves and
 574 swells co-exist under high winds. Such nonequilibrium wave motions can influence
 575 wave slope, roughness length, and wind stress (Janssen, 1991; Rieder et al., 1994;
 576 Zou et al., 2019; Patton et al., 2019; Porchetta et al., 2021; Deskos et al., 2021).
 577 Here, we attempt to incorporate the directionality of the wind and waves following
 578 Patton et al. (2019) and Porchetta et al. (2019), such that

$$z_{rough} = H_s D \cos(a\theta) \left(\frac{u_*}{c_p}\right)^{B \cos(b\theta)}. \quad (13)$$

579 D and B are the coefficients taken from COARE3.5 (See Eq. 8), while the
 580 coefficients $a = 0.4$ and $b = 0.32$ are adopted from (Porchetta et al., 2019). In prin-
 581 ciple, all these coefficients require site-specific tunings. For example, (Porchetta et
 582 al., 2019) used the high wind conditions observed from the FINO platform in the
 583 North Sea and the Air-Sea Interaction Tower (ASIT) in the New England Shelf,
 584 which represents different wind speed and wave age conditions from the trade-wind
 585 and swell-dominated tropical oceans as in the ATOMIC domain. Additional tun-
 586 ing exploiting direct momentum flux measurements would be needed to develop a
 587 refined set of coefficients for the tropical oceans. This is beyond the scope of the
 588 study. Using this new formulation, we conducted an additional coupled experiment,
 589 dubbed $WBF_θ$, which is to be compared to the default wave-based formulation in
 590 COARE3.5, where $θ = 0$.

591 Figure 13a compares the parameterized τ , color-coded by the angle (θ) be-
 592 tween the wind direction and peak wave direction in WBF. It shows that the lower
 593 τ from WBF compared to WSDF (and also observations) occurs when the swell
 594 waves are strongly misaligned with winds (e.g., $\theta > 60\text{-}90^\circ$). This indicates that
 595 the assumption of $\theta = 0$ in WBF can be attributed to the lower τ . When the di-
 596 rectional misalignments are considered in the roughness length parameterization in
 597 COARE3.5 (Figure 13b), τ over the misaligned waves has been effectively elevated
 598 as the waves opposing the wind increase the surface drag. This is shown to reduce
 599 the low τ bias significantly.

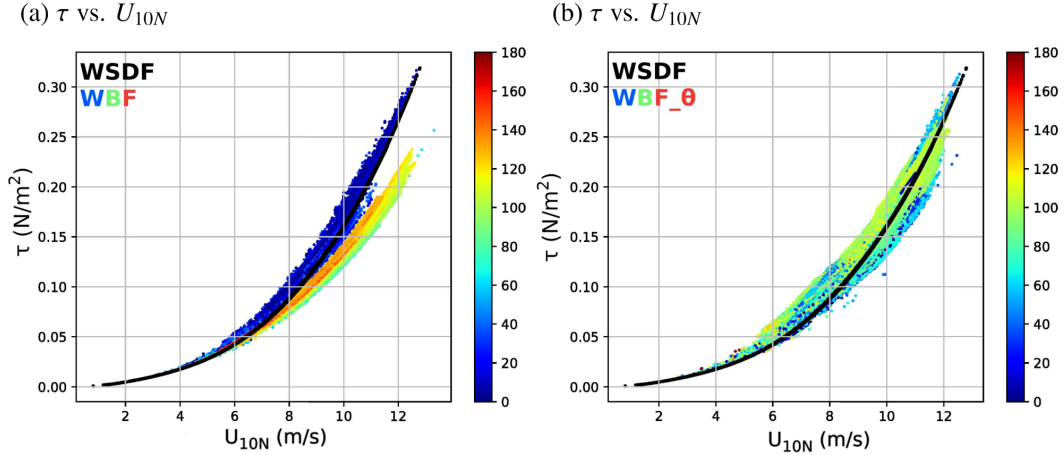


Figure 13. (a) Scatter plot of parameterized τ (Nm^{-2}) vs. U_{10N} (ms^{-1}) from WSDF in black and WBF color-coded to denote the corresponding wind-wave angle (θ) on January 8, 2020 at 0600UTC. Note that in the z_0 formulation in WBF assumes $\theta = 0$. (b) As in (a) except from WBF $_{\theta}$, where θ is treated as a non-zero quantity in the z_0 formulation.

6 Conclusion

This study investigated the role of surface waves in surface roughness length (z_0) and surface stress (τ) in the persistent and strong trade winds and swell-dominated Northwestern Atlantic Ocean during the boreal winter season. The main objective is to evaluate how accurately the air-sea momentum flux is represented in advanced bulk flux algorithms such as COARE3.5 when compared to the direct surface flux measurements. The study then identifies the wind speed and wave age regimes where the wave-based formulation (WBF) in the COARE3.5 exhibits deficiencies, and explores possible approaches to mitigating the deficiencies. In this investigation, estimated z_0 and τ from four different SCOAR ocean-atmosphere-wave coupled model simulations are compared to each other and with direct observations over the range of observed wind speeds and wave ages. These experiments are identical except for the z_0 formulation in COARE3.5.

To facilitate the unambiguous identification of the immediate impacts of different z_0 formulations without contribution from the feedback effects which affect the state variables, the two short simulations from WSDF and WBF are compared first. The results show that the estimated z_0 and τ differences strongly depend on wind speeds and wave age regimes. In the case of wind sea or fully-developed sea, the incorporation of the wave impacts via wave age and wave slope increases z_0 (Figure 4d) and τ (Figure 6b). The increase is expected, since the young seas under high winds are characterized by the enhanced wave slope and choppy surface (Figure 5b), which effectively increases the surface drag, and τ . The increased surface drag decelerates the near-surface winds (Figure 6c), consistent with the positive change in wind work due to the inclusion of waves (Figure 6d).

However, in the mixed sea condition, where moderate to high wind speeds (10 to 12 ms^{-1}) co-occur with decaying swell, the WBF tends to underestimate z_0 compared to the WSDF and τ compared to the measurements. The weak stress then accelerates the near-surface wind speed by 5% over the region of negative change in wind work (Figure 6d). The sea state in this high wave age is characterized by an aerodynamically smooth sea surface with a low wave slope (Figure 5b) and strongly

630 misaligned waves with local winds (Figure 5d), indicating the presence of remotely-
 631 generated swell. However, despite the swell-dominated sea state, the observations
 632 suggest that the wind seas in this mixed sea condition should continue to support
 633 the momentum flux due to moderate-to-high wind speeds, thereby increasing τ with
 634 wind speed (Figure 7). The current COARE3.5 WBF, on the other hand, overem-
 635 phasizes the role of swell on z_0 and predicts a decreased τ under moderate wind
 636 conditions.

637 The different approaches were explored in this study to alleviate the low-stress
 638 bias in the COARE3.5 WBF under the mixed sea regime. The first approach in-
 639 volves re-defining wave age using the mean period of the waves to better represent
 640 the wave period in the mixed sea condition (Figure 4a). The second approach takes
 641 advantage of the fully coupled model by considering the directionality of waves with
 642 respect to winds (Eq. 12), the vital missing process in the current COARE3.5 WBF
 643 and many numerical modeling studies except for a limited number of Large Eddy
 644 Simulations (LES) and offshore wind energy studies (See Review by Patton et al.,
 645 2019). Our results show that both approaches produce equivalent results by effec-
 646 tively boosting z_0 and τ under the misaligned waves under moderate-to-high winds.

647 Our analysis reveals a notable deficiency in the ocean-wave and wave-
 648 atmosphere coupling components of the coupled model, which guides the direction
 649 of our future investigation. That is, the frequency of swell simulated by the coupled
 650 WW3 model is overestimated compared to the in situ observations (Figure 8a), more
 651 so with the use of peak wave period but nonetheless noticeable with the use of mean
 652 period. Since the wave model provide the parameters required by the WBF, some
 653 of the issues described above are a result of inaccurate inputs as well as problems
 654 with the parameterization. The tendency toward the higher wave age indicates that
 655 the model under-represents critical dissipation mechanisms of the swell energy, and
 656 waves in general, which likely have contributed to the low-stress bias. There are at
 657 least two possible factors to consider.

658 First, the primary loss of swell energy is to the atmosphere in situations where
 659 the swell waves outrun the winds or propagate in the opposite direction to the lo-
 660 cal wind (e.g., Donelan, 1999; Raschle et al., 2008; Kahma et al., 2016; Liu et al.,
 661 2017). Tropical oceans, including our study region, have many low-wind regimes,
 662 where the wave-driven low-level wind jet (Harris, 1966) and turbulent mixing in the
 663 MABL (Kantha, 2006; Ardhuin & Jenkins, 2006; Babanin, 2006) constitute impor-
 664 tant sources for attenuation of the swell energy (Ardhuin et al., 2009; S. Chen et al.,
 665 2019). It is quite possible that the processes related to the upward flux of momen-
 666 tum and energy over swell are not adequately captured in our coupled wind-wave
 667 model. Previous studies find that the wave-driven wind jet is at heights of 5-10 m
 668 (Sullivan et al., 2008; Smedman et al., 2009). However, our experiments used the
 669 default vertical grid system in WRF, where the wind at the lowest height of the
 670 model is typically 30–50 m. The WRF PBL scheme expects this level to be within
 671 the constant-flux layer, where similarity theory is applied (Aligo et al., 2009; Shin
 672 et al., 2012). Yet, this level can be above the surface layer, especially in the low-
 673 wind and stable boundary layer conditions, as often observed in the northern part
 674 of the ATOMIC domain. If the turbulent mixing between the lowest model level
 675 and the swell at the sea surface is weak, the upward energy and momentum fluxes
 676 from the swell to the wind are likely to be under-represented. This might have been
 677 exacerbated by using a local PBL scheme (MYNN) in our model.

678 Moreover, parameterizations for the so-called negative wind input exist in
 679 standalone WW3 model through the use of the source term packages of wind input
 680 (Donelan et al., 2006; Ardhuin et al., 2010; Babanin, 2011; Rogers et al., 2012; Liu
 681 et al., 2017, 2019). With this, the standalone WW3 model forced with winds should
 682 better capture the loss of energy of swell waves. Yet, it is unclear how such parame-

683 terizations should be incorporated into the coupled model, as they do not represent
 684 the actual gain of momentum by the wind from the swell. Our future work will focus
 685 on adequately representing the near-surface wind responses to swell waves in the
 686 atmospheric model.

687 Secondly, the wave breaking and the induced near-surface mixing would influ-
 688 ence the wave energy growth and attenuation (e.g., Kudryavtsev et al., 2014).
 689 Also, Iyer et al. (2022), using the SWIFT drifters deployed during the ATOMIC
 690 campaign, showed that wave-current interactions can generate significant spatial
 691 and temporal variability in momentum fluxes in this region. However here, since the
 692 current study does not include wave-ocean coupling, the question about the impacts
 693 of ocean-wave coupling on the skill of the simulated wave fields cannot be addressed.
 694 This is a subject of ongoing efforts.

695 7 Open Research

696 The observational datasets from the ATOMIC and EUREC⁴A experiments are
 697 available from <https://observations.ipsl.fr/aeris/eurec4a/\#/>. ERA5 At-
 698 mospheric hourly reanalyses were made available by the Copernicus Climate Change
 699 Service (Hersbach et al., 2018a, 2018b); Mercator Ocean International daily analyses
 700 were made available by the Copernicus Marine Environment Monitoring Service:
 701 (dataset: <https://doi.org/10.48670/moi-00016>, last access: 31 January 2022);
 702 global 3-hourly spectral wave analyses were made available by Ifremer (dataset:
 703 <ftp://ftp.ifremer.fr/ifremer/ww3/HINDCAST/GLOBAL>, last access: 31 January
 704 2022); SO-HYBAM (Amazon Basin Water Resources Observation Service) data are
 705 freely available upon registration at <https://hybam.obs-mip.fr>.

706 WaveWatchIII model is distributed using GitHub ([https://github.com/
 707 NOAA-EMC/WW3](https://github.com/NOAA-EMC/WW3), last access: 31 January 2022). WRF model is distributed using
 708 GitHub (<https://github.com/wrf-model/WRF>, last access: 31 January 2022).
 709 ROMS model is freely available upon registration at <https://www.myroms.org/>.
 710 The SCOAR code is available through the GitHub repository: [https://github
 711 .com/hyodae-seo/SCOAR](https://github.com/hyodae-seo/SCOAR).

712 Acknowledgments

713 This research was supported by NOAA (NA19OAR4310376), NASA
 714 (80NSSC21K1524), and NSF (OCE-2148120). HS also acknowledges the additional
 715 support from NSF (OCE-2022846) and NOAA (NA17OAR4310255). The computing
 716 resources were provided by the WHOI High-Performance Computing Facility. The
 717 authors thank the ATOMIC and EUREC⁴A team for providing the observational
 718 datasets (<https://observations.ipsl.fr/aeris/eurec4a/\#/>). The authors also thank
 719 Elizabeth Thompson, Jim Thomson, Suneil Iyer, Ludovic Bariteau, Kyla Drushka,
 720 Chris Fairall and Denis Bourras for their insightful comments.

721 References

- 722 Aligo, E. A., Gallus, W. A., & Segal, M. (2009). On the impact of WRF model ver-
 723 tical grid resolution on Midwest summer rainfall forecasts. *Wea. Forecasting*,
 724 *24*, 575–594.
- 725 Ardhuin, F., Chapron, B., & Collard, F. (2009). Observation of swell dissipation
 726 across oceans. *Geophys. Res. Lett.*, *36*(6). doi: 10.1029/2008GL037030
- 727 Ardhuin, F., & Jenkins, A. D. (2006). On the Interaction of Surface Waves and
 728 Upper Ocean Turbulence. *Journal of Physical Oceanography*, *36*(3), 551 - 557.
 729 doi: 10.1175/JPO2862.1
- 730 Ardhuin, F., O'Reilly, W. C., Herbers, T. H. C., & Jessen, P. F. (2003). Swell

- 731 Transformation across the Continental Shelf. Part I: Attenuation and
 732 Directional Broadening. *J. Phys. Oceanogr.*, 33(9), 1921-1939. doi:
 733 10.1175/1520-0485(2003)033<1921:STATCS>2.0.CO;2
- 734 Ardhuin, F., Rogers, E., Babanin, A. V., Filipot, J.-F., Magne, R., Roland, A., ...
 735 Collard, F. (2010). Semiempirical Dissipation Source Functions for Ocean
 736 Waves. Part I: Definition, Calibration, and Validation. *J. Phys. Oceanogr.*,
 737 40(9), 1917-1941. doi: 10.1175/2010JPO4324.1
- 738 Ardhuin, F., & Roland, A. (2012). Coastal wave reflection, directional spread,
 739 and seismoacoustic noise sources. *J. Geophys. Res.*, 117(C11). doi:
 740 10.1029/2011JC007832
- 741 Babanin, A. V. (2006). On a wave-induced turbulence and a wave-mixed upper
 742 ocean layer. *Geophysical Research Letters*, 33(20). doi: [https://doi.org/10](https://doi.org/10.1029/2006GL027308)
 743 [.1029/2006GL027308](https://doi.org/10.1029/2006GL027308)
- 744 Babanin, A. V. (2011). *Breaking and Dissipation of Ocean Surface Waves*. Cam-
 745 bridge University Press. doi: 10.1017/CBO9780511736162
- 746 Battjes, J., & Janssen, J. (1978, Jan.). Energy loss and set-up due to breaking of
 747 random waves. *Coastal Engineering Proceedings*, 1, 32. doi: 10.9753/icce.v16
 748 .32
- 749 Bourras, D., Branger, H., Luneau, C., Reverdin, G., Speich, S., Geykens, N.,
 750 ... Cl  men  on, A. (2020). EUREC4A-OA_OCARINA : OCARINA
 751 Air-Sea Flux Data. *SEANOE*. (Accessed 23 December 2021) doi:
 752 <https://doi.org/10.17882/77479>
- 753 Bourras, D., Geyskens, N., Reverdin, G., Cl  men  on, A., Barrois, H., Branger, H., &
 754 Luneau, C. (2020). EUREC4A-OA experiment: Air-Sea Flux Mast Data. *SEA-*
 755 *NOE*. (Accessed 23 December 2021) doi: <https://doi.org/10.17882/77341>
- 756 Charnock, H. (1955). Wind stress on a water surface. *Quart. J. Roy. Meteor. Soc.*,
 757 81(350), 639-640. doi: 10.1002/qj.49708135027
- 758 Chen, F., & Dudhia, J. (2001). Coupling an Advanced Land Surface-Hydrology
 759 Model with the Penn State-NCAR MM5 Modeling System. Part I: Model Im-
 760 plementation and Sensitivity. *Monthly Weather Review*, 129(4), 569 - 585. doi:
 761 10.1175/1520-0493(2001)129<0569:CAALSH>2.0.CO;2
- 762 Chen, S., Qiao, F., Jiang, W., Guo, J., & Dai, D. (2019). Impact of Surface Waves
 763 on Wind Stress under Low to Moderate Wind Conditions. *Journal of Physical*
 764 *Oceanography*, 49(8), 2017 - 2028. doi: 10.1175/JPO-D-18-0266.1
- 765 Chen, S. S., Zhao, W., Donelan, M. A., & Tolman, H. L. (2013). Directional
 766 wind-wave coupling in fully coupled atmosphere-wave-ocean models: Re-
 767 sults from cblast-hurricane. *Journal of the Atmospheric Sciences*, 70(10), 3198
 768 - 3215. doi: 10.1175/JAS-D-12-0157.1
- 769 Chou, M.-D., & Suarez, M. J. (1999). A Solar Radiation Parameterization for Atmo-
 770 spheric Studies. *Technical Report Series on Global Modeling and Data Assimila-*
 771 *tion*, 15.
- 772 Colosi, L. V., Villas B  as, A. B., & Gille, S. T. (2021). The seasonal cy-
 773 cle of significant wave height in the ocean: Local versus remote forcing.
 774 *Journal of Geophysical Research: Oceans*, 126(8), e2021JC017198. doi:
 775 <https://doi.org/10.1029/2021JC017198>
- 776 Csanady, G. T., & Gibson, M. (2001). *Air-Sea Interaction: Laws and Mechanisms*.
 777 Cambridge University Press. doi: 10.1017/CBO9781139164672
- 778 Deskos, G., Lee, J. C. Y., Draxl, C., & Sprague, M. A. (2021). "review of wind-wave
 779 coupling models for large-eddy simulation of the marine atmospheric bound-
 780 ary layer". *Journal of the Atmospheric Sciences*, 78(10), 3025 - 3045. doi:
 781 10.1175/JAS-D-21-0003.1
- 782 Donelan, M. A. (1999). Wind-induced growth and attenuation of laboratory waves.
 783 *In: Institute of Mathematics and Its Applications Conference Series*, 69, Ox-
 784 ford;Clarendon, 183-194.
- 785 Donelan, M. A., Babanin, A. V., Young, I. R., & Banner, M. L. (2006). Wave-

- 786 Follower Field Measurements of the Wind-Input Spectral Function. Part II:
787 Parameterization of the Wind Input. *Journal of Physical Oceanography*, 36(8),
788 1672 - 1689. doi: 10.1175/JPO2933.1
- 789 Drennan, W. M., Graber, H. C., Hauser, D., & Quentin, C. (2003). On the wave
790 age dependence of wind stress over pure wind seas. *Journal of Geophysical Re-*
791 *search: Oceans*, 108(C3). doi: <https://doi.org/10.1029/2000JC000715>
- 792 Edson, J. B., Jampana, V., Weller, R., Bigorre, S., Plueddemann, A., Fairall,
793 C., ... Hersbach, H. (2013). On the exchange of momentum over the
794 open ocean. *Journal of Physical Oceanography*, 43(8), 1589 - 1610. doi:
795 10.1175/JPO-D-12-0173.1
- 796 Edson, J. B., Jampana, V., Weller, R. A., Bigorre, S. P., Plueddemann, A. J.,
797 Fairall, C. W., ... Hersbach, H. (2014). Corrigendum. *Journal of*
798 *Physical Oceanography*, 44(9), 2590 - 2590. Retrieved from [https://](https://journals.ametsoc.org/view/journals/phoc/44/9/jpo-d-14-0140.1.xml)
799 journals.ametsoc.org/view/journals/phoc/44/9/jpo-d-14-0140.1.xml
800 doi: 10.1175/JPO-D-14-0140.1
- 801 Egbert, G. D., & Erofeeva, S. Y. (2002). Efficient inverse modeling of barotropic
802 ocean tides. *Journal of Atmospheric and Oceanic Technology*, 19(2), 183 - 204.
803 doi: 10.1175/1520-0426(2002)019<0183:EIMOBO>2.0.CO;2
- 804 Fairall, C. W., Bradley, E. F., Hare, J. E., Grachev, A. A., & Edson, J. B. (2003).
805 Bulk parameterization of air-sea fluxes : Updates and verification for the
806 COARE algorithm. *Journal of Climate*, 16, 571-591.
- 807 Fairall, C. W., Bradley, E. F., Rogers, D. P., Edson, J. B., & Young, G. S. (1996).
808 Bulk parameterization of air-sea fluxes for tropical ocean-global atmosphere
809 coupled-ocean atmosphere response experiment. *Journal of Geophysical Re-*
810 *search: Oceans*, 101(C2), 3747-3764. doi: <https://doi.org/10.1029/95JC03205>
- 811 Hanley, K. E., & Belcher, S. E. (2008). Wave-Driven Wind Jets in the Marine At-
812 mospheric Boundary Layer. *Journal of the Atmospheric Sciences*, 65(8), 2646 -
813 2660. doi: 10.1175/2007JAS2562.1
- 814 Harris, D. L. (1966). The Wave-Driven Wind. *Journal of Atmospheric Sciences*,
815 23(6), 688 - 693. doi: 10.1175/1520-0469(1966)023<0688:TWDW>2.0.CO;2
- 816 Hasselmann, S., Hasselmann, K., Allender, J. H., & Barnett, T. P. (1985). Compu-
817 tations and Parameterizations of the Nonlinear Energy Transfer in a Gravity-
818 Wave Spectrum. Part II: Parameterizations of the Nonlinear Energy Transfer
819 for Application in Wave Models. *J. Phys. Oceanogr.*, 15(11), 1378-1391. doi:
820 10.1175/1520-0485(1985)015<1378:CAPOTN>2.0.CO;2
- 821 Hersbach, H., Bell, B., Berrisford, P., Biavati, G., Horányi, A., Muñoz Sabater,
822 J., ... Thépaut, J.-N. (2018a). ERA5 hourly data on pressure lev-
823 els from 1979 to present. Copernicus Climate Change Service (C3S) Cli-
824 mate Data Store (CDS). *Dataset*. (Accessed 01 January 2022) doi:
825 <https://doi.org/10.24381/cds.bd0915c6>
- 826 Hersbach, H., Bell, B., Berrisford, P., Biavati, G., Horányi, A., Muñoz Sabater, J.,
827 ... Thépaut, J.-N. (2018b). ERA5 hourly data on single levels from 1979
828 to present. Copernicus Climate Change Service (C3S) Climate Data Store
829 (CDS). *Dataset*. (Accessed 01 January 2022) doi: [https://doi.org/10.24381/](https://doi.org/10.24381/cds.adbb2d47)
830 [cds.adbb2d47](https://doi.org/10.24381/cds.adbb2d47)
- 831 Hong, S.-Y., & Lim, J.-O. J. (2006). The WRF Single-Moment 6-Class Microphysics
832 Scheme (WSM6). *Journal of the Korean Meteorological Society*, 42, 129-151.
- 833 Iyer, S., Thomson, J., Thompson, E., & Drushka, K. (2022). Variations in wave
834 slope and momentum flux from wave-current interactions in the tropical trade
835 winds. *Journal of Geophysical Research: Oceans*, 127(3), e2021JC018003. doi:
836 <https://doi.org/10.1029/2021JC018003>
- 837 Iyer, S., Thomson, J., Thompson, E. J., & Drushka, K. (2021). Variations
838 in wave slope and momentum flux from wave-current interactions in the
839 tropical trade winds. *Earth and Space Science Open Archive*, 51. doi:
840 10.1002/essoar.10508004.1

- 841 Janssen, P. A. E. M. (1989). Wave-induced stress and the drag of air flow over sea
842 waves. *Journal of Physical Oceanography*, *19*(6), 745 - 754. doi: 10.1175/1520-
843 -0485(1989)019(0745:WISATD)2.0.CO;2
- 844 Janssen, P. A. E. M. (1991). Quasi-linear theory of wind-wave generation applied to
845 wave forecasting. *J. Phys. Oceanogr.*, *21*(11), 1631-1642.
- 846 Jiang, H., & Chen, G. (2013). A Global View on the Swell and Wind Sea Climate
847 by the Jason-1 Mission: A Revisit. *Journal of Atmospheric and Oceanic Tech-*
848 *nology*, *30*(8), 1833 - 1841. doi: 10.1175/JTECH-D-12-00180.1
- 849 Jiménez, P. A., Dudhia, J., González-Rouco, J. F., Navarro, J., Montávez, J. P.,
850 & García-Bustamante, E. (2012). A Revised Scheme for the WRF Sur-
851 face Layer Formulation. *Monthly Weather Review*, *140*(3), 898 - 918. doi:
852 10.1175/MWR-D-11-00056.1
- 853 Kahma, K. K., Donelan, M. A., Drennan, W. M., & Terray, E. A. (2016). Evi-
854 dence of Energy and Momentum Flux from Swell to Wind. *Journal of Physical*
855 *Oceanography*, *46*(7), 2143 - 2156. doi: 10.1175/JPO-D-15-0213.1
- 856 Kantha, L. (2006). A note on the decay rate of swell. *Ocean Modelling*, *11*(1), 167-
857 173. doi: <https://doi.org/10.1016/j.ocemod.2004.12.003>
- 858 Kudryavtsev, V., Chapron, B., & Makin, V. (2014). Impact of wind waves on the
859 air-sea fluxes: A coupled model. *Journal of Geophysical Research: Oceans*,
860 *119*(2), 1217-1236. doi: <https://doi.org/10.1002/2013JC009412>
- 861 Large, W. G., McWilliams, J. C., & Doney, S. C. (1994). Oceanic vertical mixing: A
862 review and a model with a nonlocal boundary layer parameterization. *Reviews*
863 *of Geophysics*, *32*(4), 363-403. doi: <https://doi.org/10.1029/94RG01872>
- 864 Lellouche, J.-M., Greiner, E., Le Galloudec, O., Garric, G., Regnier, C., Drevillon,
865 M., ... Le Traon, P.-Y. (2018). Recent updates to the Copernicus Marine
866 Service global ocean monitoring and forecasting real-time 1/12° high-resolution
867 system. *Ocean Science*, *14*(5), 1093–1126. doi: 10.5194/os-14-1093-2018
- 868 Liu, Q., Babanin, A., Fan, Y., Zieger, S., Guan, C., & Moon, I.-J. (2017). Nu-
869 merical simulations of ocean surface waves under hurricane conditions: As-
870 sessment of existing model performance. *Ocean Modelling*, *118*, 73-93. doi:
871 <https://doi.org/10.1016/j.ocemod.2017.08.005>
- 872 Liu, Q., Rogers, W. E., Babanin, A. V., Young, I. R., Romero, L., Zieger, S., ...
873 Guan, C. (2019). Observation-based source terms in the third-generation wave
874 model wavewatch iii: Updates and verification. *Journal of Physical Oceanogra-*
875 *phy*, *49*(2), 489 - 517. doi: 10.1175/JPO-D-18-0137.1
- 876 Marshall, J., Ferrari, R., Forget, G., Maze, G., Andersson, A., Bates, N., ...
877 Thomas, L. (2009). The Climode Field Campaign: Observing the Cy-
878 cle of Convection and Restratification over the Gulf Stream. *Bulletin of*
879 *the American Meteorological Society*, *90*(9), 1337 - 1350. doi: 10.1175/
880 2009BAMS2706.1
- 881 Moon, I.-J., Hara, T., Ginis, I., Belcher, S. E., & Tolman, H. L. (2004). Effect of
882 surface waves on air-sea momentum exchange. part i: Effect of mature and
883 growing seas. *Journal of the Atmospheric Sciences*, *61*(19), 2321 - 2333. doi:
884 10.1175/1520-0469(2004)061<2321:EOSWOA>2.0.CO;2
- 885 Nakanishi, M., & Niino, H. (2004). An Improved Mellor–Yamada Level-3 Model
886 with Condensation Physics: Its Design and Verification. *Boundary-Layer Mete-*
887 *orology*, *112*, 1-31. doi: 10.1023/B:BOUN.0000020164.04146.98
- 888 Nakanishi, M., & Niino, H. (2006). An Improved Mellor–Yamada Level-3
889 Model: Its Numerical Stability and Application to a Regional Predic-
890 tion of Advection Fog. *Boundary-Layer Meteorology*, *119*, 397-407. doi:
891 10.1007/s10546-005-9030-8
- 892 Nakanishi, M., & Niino, H. (2009). Development of an improved turbulence closure
893 model for the atmospheric boundary layer. *Journal of the Meteorological Soci-*
894 *ety of Japan. Ser. II*, *87*(5), 895-912. doi: 10.2151/jmsj.87.895
- 895 Oost, W., Komen, G., Jacobs, C., & Van Oort, C. (2002). New evidence for a

- 896 relation between wind stress and wave age from measurements during AS-
 897 GAMAGE. *Boundary-Layer Meteorology volume, 103*(3), 409 - 438. doi:
 898 10.1023/A:1014913624535
- 899 Patton, E. G., Sullivan, P. P., Kosović, B., Dudhia, J., Mahrt, L., Žagar, M., &
 900 Marić, T. (2019). On the influence of swell propagation angle on surface drag.
 901 *Journal of Applied Meteorology and Climatology, 58*(5), 1039 - 1059. doi:
 902 10.1175/JAMC-D-18-0211.1
- 903 Phillips, O. M. (1985). Spectral and statistical properties of the equilibrium range in
 904 wind-generated gravity waves. *Journal of Fluid Mechanics, 156*, 505–531. doi:
 905 10.1017/S0022112085002221
- 906 Porchetta, S., Temel, O., Muñoz Esparza, D., Reuder, J., Monbaliu, J., van Beeck,
 907 J., & van Lipzig, N. (2019). A new roughness length parameterization ac-
 908 counting for wind–wave (mis)alignment. *Atmospheric Chemistry and Physics,*
 909 *19*(10), 6681–6700. doi: 10.5194/acp-19-6681-2019
- 910 Porchetta, S., Temel, O., Warner, J., Muñoz-Esparza, D., Monbaliu, J., van Beeck,
 911 J., & van Lipzig, N. (2021). Evaluation of a roughness length parametrization
 912 accounting for wind–wave alignment in a coupled atmosphere–wave model.
 913 *Quarterly Journal of the Royal Meteorological Society, 147*(735), 825–846. doi:
 914 <https://doi.org/10.1002/qj.3948>
- 915 Quinn, P. K., Thompson, E. J., Coffman, D. J., Baidar, S., Bariteau, L., Bates,
 916 T. S., ... Zuidema, P. (2021). Measurements from the RV *Ronald H. Brown*
 917 and related platforms as part of the Atlantic Tradewind Ocean-Atmosphere
 918 Mesoscale Interaction Campaign (ATOMIC). *Earth System Science Data,*
 919 *13*(4), 1759–1790. doi: 10.5194/essd-13-1759-2021
- 920 Rasche, N., & Ardhuin, F. (2013). A global wave parameter database for geophysical
 921 applications. Part 2: Model validation with improved source term parame-
 922 terization. *Ocean Modelling, 70*, 174 - 188. (Ocean Surface Waves) doi:
 923 10.1016/j.ocemod.2012.12.001
- 924 Rasche, N., Ardhuin, F., Queffelec, P., & Croizé-Fillon, D. (2008). A global
 925 wave parameter database for geophysical applications. part 1: Wave-
 926 current–turbulence interaction parameters for the open ocean based on
 927 traditional parameterizations. *Ocean Modelling, 25*(3), 154–171. doi:
 928 <https://doi.org/10.1016/j.ocemod.2008.07.006>
- 929 Renault, L., McWilliams, J. C., & Penven, P. (2017). Modulation of the Agulhas
 930 Current Retroflexion and Leakage by Oceanic Current Interaction with the
 931 Atmosphere in Coupled Simulations. *Journal of Physical Oceanography, 47*(8),
 932 2077 - 2100. doi: 10.1175/JPO-D-16-0168.1
- 933 Renault, L., Molemaker, M. J., Gula, J., Masson, S., & McWilliams, J. C. (2016).
 934 Control and Stabilization of the Gulf Stream by Oceanic Current Interaction
 935 with the Atmosphere. *Journal of Physical Oceanography, 46*(11), 3439 - 3453.
 936 doi: 10.1175/JPO-D-16-0115.1
- 937 Rieder, K. F., Smith, J. A., & Weller, R. A. (1994). Observed directional charac-
 938 teristics of the wind, wind stress, and surface waves on the open ocean. *Jour-
 939 nal of Geophysical Research: Oceans, 99*(C11), 22589–22596. doi: [https://doi
 940 .org/10.1029/94JC02215](https://doi.org/10.1029/94JC02215)
- 941 Rogers, W. E., Babanin, A. V., & Wang, D. W. (2012). Observation-Consistent
 942 Input and Whitecapping Dissipation in a Model for Wind-Generated Surface
 943 Waves: Description and Simple Calculations. *Journal of Atmospheric and
 944 Oceanic Technology, 29*(9), 1329 - 1346. doi: 10.1175/JTECH-D-11-00092.1
- 945 Sauvage, C., Lebeaupin Brossier, C., Bouin, M.-N., & Ducrocq, V. (2020). Charac-
 946 terization of the air–sea exchange mechanisms during a Mediterranean heavy
 947 precipitation event using realistic sea state modelling. *Atmos. Chem. Phys.,*
 948 *20*(3), 1675–1699. doi: 10.5194/acp-20-1675-2020
- 949 Semedo, A., Sušelj, K., Rutgersson, A., & Sterl, A. (2011). A Global View on
 950 the Wind Sea and Swell Climate and Variability from ERA-40. *Journal of*

- 951 *Climate*, 24(5), 1461 - 1479. doi: 10.1175/2010JCLI3718.1
- 952 Seo, H., Miller, A. J., & Roads, J. O. (2007, feb). The Scripps Coupled
953 Ocean–Atmosphere Regional (SCOAR) Model, with Applications in the
954 Eastern Pacific Sector. *Journal of Climate*, 20(3), 381–402. doi: 10.1175/
955 jcli4016.1
- 956 Seo, H., Song, H., O’Neill, L. W., Mazloff, M. R., & Cornuelle, B. D. (2021). Im-
957 pacts of Ocean Currents on the South Indian Ocean Extratropical Storm Track
958 through the Relative Wind Effect. *Journal of Climate*, 34(22), 9093 - 9113.
959 doi: 10.1175/JCLI-D-21-0142.1
- 960 Seo, H., Subramanian, A. C., Song, H., & Chowdary, J. S. (2019). Coupled effects of
961 ocean current on wind stress in the bay of bengal: Eddy energetics and upper
962 ocean stratification. *Deep Sea Research Part II: Topical Studies in Oceanogra-
963 phy*, 168, 104617. (Atmosphere-Ocean Dynamics of Bay of Bengal - Volume I)
964 doi: <https://doi.org/10.1016/j.dsr2.2019.07.005>
- 965 Shchepetkin, A. F., & McWilliams, J. C. (2005). The regional oceanic modeling
966 system (ROMS): a split-explicit, free-surface, topography-following-coordinate
967 oceanic model. *Ocean Modelling*, 9(4), 347-404. doi: [https://doi.org/10.1016/
968 j.ocemod.2004.08.002](https://doi.org/10.1016/j.ocemod.2004.08.002)
- 969 Shin, H. H., Hong, S.-Y., & Dudhia, J. (2012). Impacts of the Lowest Model
970 Level Height on the Performance of Planetary Boundary Layer Parame-
971 terizations. *Monthly Weather Review*, 140(2), 664 - 682. doi: 10.1175/
972 MWR-D-11-00027.1
- 973 Skamarock, W. C., Klemp, J. B., Dudhia, J., Gill, D. O., Barker, D., Duda, M. G.,
974 & Powers, J. G. (2008). *A Description of the Advanced Research WRF Version
975 3* (Tech. Rep. Nos. NCAR/TN-475+STR). doi: 10.5065/D68S4MVH
- 976 Smedman, A., Högström, U., Sahleé, E., Drennan, W. M., Kahma, K. K., Petters-
977 son, H., & Zhang, F. (2009). Observational Study of Marine Atmospheric
978 Boundary Layer Characteristics during Swell. *Journal of the Atmospheric
979 Sciences*, 66(9), 2747 - 2763. doi: 10.1175/2009JAS2952.1
- 980 Stevens, B., Bony, S., Farrell, D., Ament, F., Blyth, A., Fairall, C., ... Zöger, M.
981 (2021). EUREC⁴A. *Earth System Science Data*, 13(8), 4067–4119. doi:
982 10.5194/essd-13-4067-2021
- 983 Sullivan, P. P., Edson, J. B., Hristov, T., & McWilliams, J. C. (2008). Large-eddy
984 simulations and observations of atmospheric marine boundary layers above
985 nonequilibrium surface waves. *Journal of the Atmospheric Sciences*, 65(4),
986 1225 - 1245. doi: 10.1175/2007JAS2427.1
- 987 Taylor, P. K., & Yelland, M. J. (2001, 02). The Dependence of Sea Surface Rough-
988 ness on the Height and Steepness of the Waves. *Journal of Physical Oceanogra-
989 phy*, 31(2), 572-590. doi: 10.1175/1520-0485(2001)031<0572:TDOSSR>2.0.CO;
990 2
- 991 The WAVEWATCH III Development Group. (2016). *User manual and system
992 documentation of WAVEWATCH III version 5.16* (Tech. Rep. No. 329).
993 College Park, MD, USA: NOAA/NWS/NCEP/MMAB. Retrieved from
994 <https://polar.ncep.noaa.gov/waves/wavewatch/manual.v5.16.pdf>
- 995 Thompson, E., Fairall, C., Pezoa, S., & Bariteau, L. (2021). ATOMIC ship naviga-
996 tion, meteorology, seawater, fluxes: Near-surface meteorology, air-sea
997 fluxes, surface ocean waves, and near surface ocean parameters (tempera-
998 ture, salinity, currents) and primary dataset of ship location and navigation
999 estimated from in-situ and remote sensing instruments aboard NOAA Ship
1000 Ronald H. Brown in the North Atlantic Ocean, near Barbados: Atlantic
1001 Tradewind Ocean-Atmosphere Mesoscale Interaction Campaign 2020-01-
1002 09 to 2020-02-12 (NCEI Accession 0225427). *NOAA National Centers for
1003 Environmental Information. Dataset*. (Accessed 23 December 2021) doi:
1004 <https://doi.org/10.25921/etxb-ht19>
- 1005 Thomson, J. (2012). Wave Breaking Dissipation Observed with “SWIFT” Drifters.

- 1006 *Journal of Atmospheric and Oceanic Technology*, 29(12), 1866 - 1882. doi: 10
1007 .1175/JTECH-D-12-00018.1
- 1008 Thomson, J., Moulton, M., de Klerk, A., Talbert, J., Guerra, M., Kastner, S.,
1009 ... Nylund, S. (2019). A new version of the SWIFT platform for waves,
1010 currents, and turbulence in the ocean surface layer. In *2019 IEEE/OES*
1011 *Twelfth Current, Waves and Turbulence Measurement (CWTM)* (p. 1-7).
1012 doi: 10.1109/CWTM43797.2019.8955299
- 1013 Thomson, J., Thompson, E., Iyer, S., Drushka, K., & de Klerk, A. (2021). ATOMIC
1014 SWIFT drifters: Near-surface meteorology, air-sea fluxes, surface ocean waves,
1015 and near-surface ocean properties (turbulent dissipation rate, currents, tem-
1016 perature, salinity) estimated from in-situ and remote sensing instruments
1017 aboard six SWIFT drifters (Surface Wave Instrument Float with Tracking)
1018 launched and recovered for two different deployments from NOAA Ship
1019 Ronald H. Brown in the North Atlantic Ocean, near Barbados: Atlantic
1020 Tradewind Ocean-Atmosphere Mesoscale Interaction Campaign 2020-01-
1021 14 to 2020-02-11 (NCEI Accession 0225279). *NOAA National Centers for*
1022 *Environmental Information. Dataset.* (Accessed 23 December 2021) doi:
1023 <https://doi.org/10.25921/s5d7-tc07>
- 1024 Tolman, H. L., Balasubramanian, B., Burroughs, L. D., Chalikov, D. V., Chao,
1025 Y. Y., Chen, H. S., & Gerald, V. M. (2002). Development and Implemen-
1026 tation of Wind-Generated Ocean Surface Wave Modelsat NCEP. *Weather*
1027 *and Forecasting*, 17(2), 311 - 333. doi: 10.1175/1520-0434(2002)017<0311:
1028 DAIOWG>2.0.CO;2
- 1029 Villas Bôas, A. B., & Young, W. R. (2020). Directional diffusion of surface gravity
1030 wave action by ocean macroturbulence. *Journal of Fluid Mechanics*, 890, R3.
1031 doi: 10.1017/jfm.2020.116
- 1032 Wunsch, C. (1998). The Work Done by the Wind on the Oceanic General Circu-
1033 lation. *Journal of Physical Oceanography*, 28(11), 2332 - 2340. doi: 10.1175/
1034 1520-0485(1998)028<2332:TWDBTW>2.0.CO;2
- 1035 Zheng, Y., Alapaty, K., Herwehe, J. A., Genio, A. D. D., & Niyogi, D. (2016). Im-
1036 proving High-Resolution Weather Forecasts Using the Weather Research and
1037 Forecasting (WRF) Model with an Updated Kain-Fritsch Scheme. *Monthly*
1038 *Weather Review*, 144(3), 833 - 860. doi: 10.1175/MWR-D-15-0005.1
- 1039 Zou, Z., Song, J., Li, P., Huang, J., Zhang, J. A., Wan, Z., & Li, S. (2019). Effects
1040 of swell waves on atmospheric boundary layer turbulence: A low wind field
1041 study. *Journal of Geophysical Research: Oceans*, 124(8), 5671-5685. doi:
1042 <https://doi.org/10.1029/2019JC015153>